bioRxiv preprint doi: https://doi.org/10.1101/441659; this version posted October 13, 2018. The copyright holder for this preprint (which was not certified by peer review) is the author/funder, who has granted bioRxiv a license to display the preprint in perpetuity. It is made available under aCC-BY-NC-ND 4.0 International license.

# Does the Diffusion Tensor Model Predict the Neurite Distribution of Cerebral Cortical Gray Matter? – Cortical DTI-NODDI

**Authors:**

Hikaru Fukutomi[1,2], Matthew F. Glasser[3,4], Katsutoshi Murata[5], Thai Akasaka[2], Koji Fujimoto[2], Takayuki Yamamoto[2], Joonas A. Autio[1], Tomohisa Okada[2], Kaori Togashi[2], Hui Zhang[6], David C. Van Essen[3], Takuya Hayashi[1,7]

**Affiliations:**

[1]Laboratory for Brain Connectomics Imaging, RIKEN Center for Biosystems Dynamics Research, Kobe, Japan

[2]Department of Diagnostic Imaging and Nuclear Medicine, Kyoto University Graduate School of Medicine, Kyoto Japan

[3]Department of Neuroscience, Washington University School of Medicine, St. Louis, MO, USA

[4]Department of Radiology, Washington University School of Medicine, St. Louis, MO, USA

[5]Siemens Healthcare K.K. Japan

[6]Centre for Medical Image Computing and Department of Computer Science, University College London, UK

[7]RIKEN Compass to Healthy Life Research Complex Program, Kobe, Japan

**Corresponding author**

Takuya Hayashi, MD, PhD

Team Leader

Laboratory for Brain Connectomics Imaging

RIKEN Center for Biosystems Dynamics Research

6-7-3 Minatojima-minamimachi, Chuo-ku, Kobe 650-0047, Japan

Tel: 81-78-304-7140

Fax: 81-78-304-7141

E-mail: takuya.hayashi@riken.jp

**Key words**

neurite density, orientation dispersion, cortical mapping, diffusion tensor imaging, NODDI,

bioRxiv preprint doi: https://doi.org/10.1101/441659; this version posted October 13, 2018. The copyright holder for this preprint (which was not certified by peer review) is the author/funder, who has granted bioRxiv a license to display the preprint in perpetuity. It is made available under aCC-BY-NC-ND 4.0 International license.

**Abstract**

Diffusion tensor imaging (DTI) has been widely used in human neuroimaging, but its measures are poorly linked to neurobiological features in the gray matter, primarily due to the complexity and heterogeneity of gray matter. Previously, mean diffusivity of DTI in the cortical gray matter was shown to correlate highly with an index of neurites estimated by a recently proposed model, neurite orientation dispersion and density imaging (NODDI). NODDI explicitly models neurites and has been histologically validated. However, the generalizability of the relationship between DTI and NODDI has yet to be fully clarified. Here, we evaluate whether and how DTI can predict the cortical neurite metrics of NODDI, neurite density index (NDI) and orientation dispersion index (ODI). We generated a mathematical relationship between DTI and NODDI by assuming a negligible compartment of cerebro-spinal fluid (CSF) (DTI-NODDI); we predicted and validated quantitative values of the NDI and ODI by comparing estimates derived from DTI to the original NODDI using 456 subjects' data in the Human Connectome Project (HCP). Simulations for the error of DTI-NODDI were also performed to evaluate the impact of neglecting the CSF compartment and to characterize the effects of partial volume and heterogeneity of CSF and b-shell scheme of diffusion data. For both NDI and ODI, cortical distributions of DTI-NODDI closely resembled those in the original NODDI model, particularly when using data that included the highest diffusion weighting (b-value=3000). The DTI-NODDI values in cortical regions of interest were slightly overestimated but highly correlated with the original. Simulations confirmed that analyzing with high b-value data minimized error propagation from heterogeneity and partial voluming of CSF, although values were consistently overestimated. These findings suggest that DTI can predict the variance of NODDI metrics and hence neurite distribution of cortical gray matter when using high b-value diffusion MRI data.

bioRxiv preprint doi: https://doi.org/10.1101/441659; this version posted October 13, 2018. The copyright holder for this preprint (which was not certified by peer review) is the author/funder, who has granted bioRxiv a license to display the preprint in perpetuity. It is made available under aCC-BY-NC-ND 4.0 International license.

## 1. Introduction

The diffusion motion of water molecules in brain tissue is affected by the local microarchitecture, including axons, dendrites and cell bodies (Moseley et al., 1990). Diffusion tensor imaging (DTI) is a well established model that describes Gaussian properties of diffusion motion in a fibrous structure like brain white matter (Basser et al., 1994a, 1994b) and is widely used for inferring the microstructural changes related to plasticity and diseases (for review, Johansen-Berg and Behrens, 2013). In most cases, summary parameters of DTI, fractional anisotropy (FA) and mean diffusivity (MD), have been studied, however, these parameters have not been shown to be specific to underlying microstructural features of axons and dendrites (collectively referred to as neurites) and are often sensitive to tissue compartments other than neurites (Pierpaoli and Basser, 1996). DTI analyses often fail to capture the specifically varying features of underlying microstructure; e.g. a decrease in FA may be caused by an increase in the dispersion of neurite orientation, a decrease in neurite density, or another tissue microstructural change (Jones and Cercignani, 2010; Pierpaoli et al., 1996; Pierpaoli and Basser, 1996). In particular, using DTI in gray matter tissue is thought to be inaccurate due to the complexity and heterogeneity of gray matter diffusion (Assaf, 2018). Despite that, recent DTI studies suggest potential microstructural changes in the gray matter of patients with multiple sclerosis and Alzheimer's disease (Calabrese et al., 2011; Eustache et al., 2016; Henf et al., 2018), though the findings are yet to be associated with specific pathological changes. Therefore, it is worth addressing the issue of how closely DTI measures are associated with the underlying complexity of the gray matter microstructure, particularly those related to neurite properties.

One recent advance for estimating the microstructural complexity of brain tissue using diffusion MRI (dMRI) is the Neurite Orientation Dispersion and Density Imaging (NODDI) (Zhang et al., 2012). NODDI models dMRI signals by combining three tissue compartments: neurites, extra-neurites, and cerebro-spinal fluid (CSF), each with different properties of diffusion motion, and enables in vivo estimation of a neurite density index (NDI) and an orientation dispersion index (ODI), as well as a volume fraction of isotropic diffusion ($V_{iso}$). NODDI requires dMRI data to be scanned with relatively higher number of diffusion gradient directions (e.g. >90 directions) and b-values (e.g. b=700 and 2000 sec/mm$^2$) as compared with DTI (Zhang et al., 2012). The NDI estimates the volume fraction of neurites, including both axons and dendrites, whereas the ODI estimates the variability of neurite orientation: ranging from 0 (all parallel) to 1 (isotropically randomly oriented). Variation of NODDI estimates in white matter have been related to aging (Billiet et al., 2015; Chang et al., 2015; Eaton-Rosen et al., 2015; Genc et al., 2017; Kodiweera et al., 2016; Kunz et al., 2014) and neurologic disorders (Adluru et al., 2014; Billiet et al., 2014; Timmers et al., 2015). Gray matter changes jn

bioRxiv preprint doi: https://doi.org/10.1101/441659; this version posted October 13, 2018. The copyright holder for this preprint (which was not certified by peer review) is the author/funder, who has granted bioRxiv a license to display the preprint in perpetuity. It is made available under aCC-BY-NC-ND 4.0 International license.

NODDI were also reported in patients with IFN-α-induced fatigue (Dowell et al., 2017), Wilson's disease (Song et al., 2017), cortical dysplasia (Winston et al., 2014), aging (Nazeri et al., 2015), and schizophrenia (Nazeri et al., 2016). Importantly, histological studies suggest that NDI is correlated with myelin (Grussu et al., 2017) and that ODI is associated with complexity of fiber orientation (Grussu et al., 2017; Sato et al., 2017; Schilling et al., 2018).

We recently optimized NODDI for cortical gray matter (Fukutomi et al., 2018), finding that the NDI is closely related to cortical myelin, as estimated by the ratio of T1w to T2w MRI images (Glasser and Van Essen, 2011) and that ODI is associated with cortical cytoarchitecture as mapped by Von Economo and Koskinas (Triarhou, 2009; von Economo and Koskinas, 1925). In addition, we found strong relationships between NODDI and DTI parameters in the cortex, in particular, NDI and 1/MD were very highly correlated (R=0.97) (Fukutomi et al., 2018). We proposed (Fukutomi et al., 2018) that this strong correlation reflects a recently derived mathematical relation between NODDI and DTI parameters (Edwards et al., 2017) (Lampinen et al., 2017). This relationship relies on the assumption that CSF compartment ($V_{iso}$) is negligible in the tissue (Edwards et al., 2017, Lampinen et al., 2017). In support of this assumption for cortical gray matter, the estimated $V_{iso}$ in the cortex, particularly when mapped on the surface, is relatively small compared to that in the white matter (Fukutomi et al., 2018). In contrast, white matter may be a major site for convective flow of CSF (Rosenberg et al., 1980).

In the present study, we evaluate whether NODDI parameters in cortical gray matter can be predicted from DTI parameters utilizing a mathematical relationship between the two models. We present a method that estimates cortical maps of NDI and ODI of NODDI based on DTI values (cortical DTI-NODDI), which is computationally less expensive than the original NODDI. We used Human Connectome Project (HCP) data that had already preprocessed. Since the estimated size of the CSF compartment may depend on b-value and spatial resolution, we evaluated the quantitative accuracy of the surface distribution of NODDI measures using different b-values of dMRI. We additionally performed simulation analysis in terms of b-value, proportion of CSF signal, and random noise in data.

## 2. Materials and Methods

We first describe the models and formulations of the original NODDI and the DTI-based estimation of NODDI (DTI-NODDI). Based on the formulation, we evaluated the DTI-NODDI model for cortical neurite estimation using *in vivo* MRI data of the HCP (https://www.humanconnectome.org/).

bioRxiv preprint doi: https://doi.org/10.1101/441659; this version posted October 13, 2018. The copyright holder for this preprint (which was not certified by peer review) is the author/funder, who has granted bioRxiv a license to display the preprint in perpetuity. It is made available under aCC-BY-NC-ND 4.0 International license.

We used publicly available data from 456 healthy subjects (aged 22-35 years) to test whether DTI-NODDI can provide as accurate neurite maps as those from the original NODDI model. In particular, dMRI datasets with different b-shell structures were analyzed to investigate how the b-shell scheme affects neurite estimations. We also performed simulation analyses to clarify how the b-shell scheme dependency of DTI-NODDI is associated with several error sources such as CSF signals in dMRI data, partial volume effects, and random noise. The reproducibility of DTI-NODDI was also assessed using test-retest HCP data. Data analyses were performed at RIKEN, and the use of HCP data in this study was approved by the institutional ethical committee (KOBE-IRB-16-24).

## 2.1 Models

### 2.1.1 *The original NODDI Model*

The NODDI method models brain microarchitecture in three compartments that have different properties of water molecules' diffusion motion: the intracellular compartment (restricted diffusion bounded by neurites), the extracellular compartment (outside of neurites and potentially including glial cells), and the CSF compartment (Zhang et al., 2012). The intracellular compartment is modeled as a set of sticks, i.e., cylinders of zero radius in which diffusion of water is highly restricted in directions perpendicular to neurites and unhindered along them (Behrens et al., 2003; Panagiotaki et al., 2012; Sotiropoulos et al., 2012). The orientation distribution of these sticks is modeled with a Watson distribution, because it is the simplest distribution that can capture the dispersion in orientations (Mardia and Jupp, 1990). The extracellular compartment is modeled with anisotropic Gaussian diffusion parallel to the main direction. The CSF compartment is modeled as isotropic Gaussian diffusion. The full normalized signal A is thus written as:

$$A= (1-V_{iso})\{V_{ic} A_{ic}+(1-V_{ic})A_{ec}\}+V_{iso} A_{iso}, \qquad (1)$$

where $A_{iso}$ and $V_{iso}$ are the normalized signal and volume fraction of the CSF compartment; the volume fraction of non-CSF compartment ($1-V_{iso}$) is further divided into intracellular compartment ($V_{ic}$) (=NDI) and extracellular compartment ($1-V_{ic}$); $A_{ic}$ and $A_{ec}$ is the normalized signal of the intracellular and extracellular compartments, respectively. Additional NODDI parameters are isotropic diffusivity ($d_{iso}$) and intrinsic free diffusivity ($d_{\parallel}$), i.e., the diffusivity parallel to neurites. Detailed expressions of mathematical equations and derivation are described in the Appendix, and these formulations were used for the simulation study described in Section 2.3.

### 2.1.2 *The DTI-based estimation of NODDI (DTI-NODDI)*

bioRxiv preprint doi: https://doi.org/10.1101/441659; this version posted October 13, 2018. The copyright holder for this preprint (which was not certified by peer review) is the author/funder, who has granted bioRxiv a license to display the preprint in perpetuity. It is made available under aCC-BY-NC-ND 4.0 International license.

The equations that relate NODDI to DTI models are detailed in previous studies (Edwards et al., 2017; Lampinen et al., 2017). Briefly, the NDI and the orientation parameter (τ) can be expressed by using DTI measures such as MD and FA in the following equations, assuming that the CSF compartment ($V_{iso}$) is negligible:

$$NDI = 1 - \sqrt{\frac{1}{2}\left(\frac{3MD}{d_{//}} - 1\right)} \qquad (2)$$

$$\tau = \frac{1}{3}\left(1 + \frac{4MD \cdot FA}{|d_{//} - MD|\sqrt{3 - 2FA^2}}\right), \qquad (3)$$

where $d_{//}$ is a constant for intrinsic diffusivity assumed in the NODDI model. The orientation dispersion index (ODI) is calculated using the following formulas:

$$\tau = \frac{1}{\sqrt{\pi\kappa}\exp(-k)erfi(\sqrt{\kappa})} - \frac{1}{2\kappa} \qquad (4)$$

$$ODI = \frac{2}{\pi}\arctan\left(\frac{1}{\kappa}\right), \qquad (5)$$

where *erfi* is the imaginary error function and *arctan* is the arctangent. Based on these equations, once we have DTI measures such as FA and MD, 1) NDI can be analytically estimated from MD using formula (2) ($NDI_{DTI}$) by using an assumed value of $d_{//}$, 2) τ can be calculated using formula (3) and values of MD and FA, 3) κ can be estimated using formula (4) by using a look-up-table and a value of τ calculated at the previous step, and 4) $ODI_{DTI}$ was calculated using the formula (5) and κ. Plotting values of DTI and predicted NODDI makes their relationship much clearer (Fig. 1). Using $d_{//}$=1.1 × $10^{-3}$ $mm^2/s$ (optimized for gray matter (Fukutomi et al., 2018)) and for an expected range of MD in the cortex (5 to 6 x $10^{-4}$ $mm^2/s$, see Fig. 4B in (Fukutomi et al., 2018)), we found that the value of NDI is predicted by a monotonically increasing function of the inverse of MD (Fig. 1A) and that ODI is a monotonically decreasing function of MD but also has a floor effect based on the value of FA (Fig. 1B).

bioRxiv preprint doi: https://doi.org/10.1101/441659; this version posted October 13, 2018. The copyright holder for this preprint (which was not certified by peer review) is the author/funder, who has granted bioRxiv a license to display the preprint in perpetuity. It is made available under aCC-BY-NC-ND 4.0 International license.

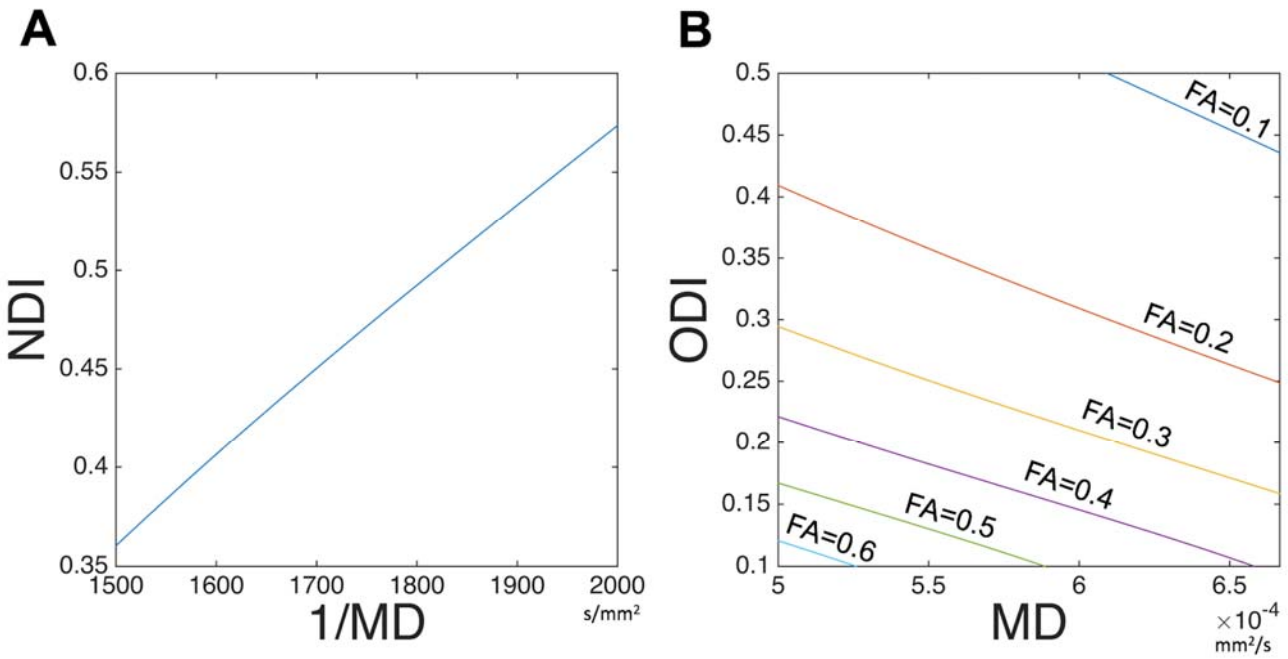


**Figure 1.** Relationships of values between NODDI and DTI based on DTI-NODDI model. The equations for DTI-NODDI (Eq. 2-5) and $d_{//} = 1.1\times10^{-3}$ mm$^2$/s (optimized for gray matter) were used to simulate relationships between **A)** Neurite density index (NDI) vs inversed mean diffusivity (1/MD), over the range of MD= 1500 to 2000 s/mm$^2$, and **B)** orientation dispersion index (ODI) vs MD when fractional anisotropy (FA) ranged from 0.1 to 0.6. Data at https://balsa.wustl.edu/r519

## 2.2 Cortical DTI-NODDI using in vivo MRI data

### 2.2.1 *Subjects and dMRI datasets*

We used the 'S500 Release Subjects' dataset from the publicly available HCP dataset, including high-resolution structural images (0.7-mm isotropic T1w and T2w images, (Glasser et al., 2013) and dMRI data (1.25-mm isotropic resolution) (Sotiropoulos et al., 2013). The dMRI data included 270 volumes with 90 volumes for each of the three shells of b-values (b=1000, 2000 and 3000 s/mm$^2$) in addition to 18 non-diffusion weighted (b=0 s/mm$^2$) volumes. From this dataset, 456 healthy subjects (age, 22-35 years) scanned with a complete dataset of 270 volumes were chosen, and 49 subjects were excluded based on incomplete dMRI scans. To investigate reproducibility, 32 subjects' retest data were used. In our previous study, NDI and the reciprocal of MD (1/MD) showed very similar surface distributions when all of the dMRI data were used, but they did not show similar distributions when only a single shell of b=1000 dMRI data was used (Fukutomi et al., 2018). Therefore, we hypothesized that the validity of DTI-NODDI may differ depending on the b-shell scheme of dMRI data. To address this, datasets with different b-shell schemes were used for analysis (Table 1), i.e. for each subject, seven types of b-shell datasets were derived from dMRI data as follows: three one-shell datasets using b=0 volume and any one of b=1000, 2000, or 3000 volume; three two-shell datasets using b=0 images and any two of b=1000, 2000, or 3000 volume; and a

bioRxiv preprint doi: https://doi.org/10.1101/441659; this version posted October 13, 2018. The copyright holder for this preprint (which was not certified by peer review) is the author/funder, who has granted bioRxiv a license to display the preprint in perpetuity. It is made available under aCC-BY-NC-ND 4.0 International license.

three-shell dataset using all images.

**Table 1** The table lists abbreviations of b-shell datasets used in the main text and corresponding datasets of dMRI in different b-shell schemes. The numbers in parentheses indicate the number of b0 volumes with repeatedly obtained for b=0 volume or diffusion weighted directions with different b-vectors (or directions of diffusion-weighted gradient) for each of the b=1000, 2000 and 3000 shells.

| Abbreviations of b-shell datasets | Datasets of non-diffusion weighted (b=0) and diffusion-weighted MRI volumes (b=1000,2000 and 3000) |
|---|---|
| $b_{1000}$ | b=0 (18), b=1000 (90) |
| $b_{2000}$ | b=0 (18), b=2000 (90) |
| $b_{3000}$ | b=0 (18), b=3000 (90) |
| $b_{1000\text{-}2000}$ | b=0 (18), b=1000 (90), b=2000 (90) |
| $b_{1000\text{-}3000}$ | b=0 (18), b=1000 (90), b=3000 (90) |
| $b_{2000\text{-}3000}$ | b=0 (18), b=2000 (90), b=3000 (90) |
| $b_{All}$ | b=0 (18), b=1000 (90), b=2000 (90), b=3000 (90) |

2.2.2 *Calculation of the cortical surface map of NODDI and DTI-NODDI parameters*

The DTI estimates (FA and MD) were calculated using each dataset of dMRI and the dtifit diffusion tensor modeling tool in Functional Magnetic Resonance Imaging of the Brain Software Library (FSL) 5.09 (http:// www.fmrib.ox.ac.uk/fsl). To compare DTI-NODDI with the original NODDI, the diffusion data were also fitted to the NODDI model using the optimized value of $d_{//}$ and Accelerated Microstructure Imaging via Convex Optimization (AMICO) 1.0 (Daducci et al., 2015), which re-formulates the original NODDI model as a linear system and shortens the calculation time. The value of $d_{//}$ was optimized for the cerebral cortex ($1.1 \times 10^{-3}$ $mm^2/s$) from the original setting value ($1.7 \times 10^{-3}$ $mm^2/s$) (Fukutomi et al., 2018), because we are interested in the cerebral cortical gray matter. We used default values of regularization ($\lambda$=0.001 and $\gamma$=0.5) for AMICO.

The parameters of the original NODDI model (NDI and $\kappa$) and the DTI model (FA and MD) were mapped onto the cortical surface, as described previously (Fukutomi et al., 2018). Briefly, the algorithm for surface mapping identifies cortical ribbon voxels within a cylinder orthogonal to the local surface for each mid-thickness surface vertex on the native mesh and weights them using a Gaussian function (FWHM= ~4 mm, $\sigma$=5/3 mm), which reduces the contribution of voxels that contain substantial partial volumes of CSF or white matter (Glasser and Van Essen 2011 Journal of Neuroscience). The $ODI_{ORIG}$ was calculated using the surface metric of $\kappa$ and equation (5). Subsequently, $NDI_{DTI}$ and $ODI_{DTI}$ maps were calculated from FA and MD maps using in-house script

bioRxiv preprint doi: https://doi.org/10.1101/441659; this version posted October 13, 2018. The copyright holder for this preprint (which was not certified by peer review) is the author/funder, who has granted bioRxiv a license to display the preprint in perpetuity. It is made available under aCC-BY-NC-ND 4.0 International license.

of DTI-NODDI written by MATLAB (R2013a) (http://www.mathworks.com/). The surface maps were resampled using MSMAll surface registration (Glasser et al., 2016; Robinson et al., 2014, 2018) and onto the 32k group average surface mesh. For surface-based analysis, we used Connectome Workbench (https://github.com/Washington-University/workbench,, Marcus et al., 2013). The tool for DTI-NODDI and NODDI surface mapping used in this manuscript is available from NoddiSurfaceMapping (https://github.com/RIKEN-BCIL/NoddiSurfaceMapping). All calculations were performed using a workstation including a 32 core CPU: Intel(R) Xeon(R) CPU E5-2687W v2 @ 3.40GHz, Memory: 128GB, DIMM DDR3 1866 MHz (0.5 ns) and operation system: Ubuntu 14.04.

2.2.3 *Statistical analysis*

Surface maps of $NDI_{ORIG}$, $ODI_{ORIG}$, $V_{iso}$, $NDI_{DTI}$ and $ODI_{DTI}$ using each dataset were averaged across subjects and parcellated using the HCP's multi-modal cortical parcellation (HCP_MMP1.0 210P MPM version) (Glasser et al., 2016). The mean value of each measure for each of the 180 parcels per hemisphere was calculated. $NDI_{ORIG}$ and $ODI_{ORIG}$ calculated using all the dMRI data were considered 'a gold standard' reference. To investigate the linear relationship between DTI-NODDI and the original NODDI, the correlations between each parcellated surface map ($NDI_{ORIG}$, $ODI_{ORIG}$, $NDI_{DTI}$ and $ODI_{DTI}$) and the reference in each subject were calculated using Pearson correlation analysis. The linear regression analysis was also performed using the reference as independent variable and DTI-NODDI as predictors. The mean of the correlation coefficient across subjects was computed after using the Fisher Z transformation. To investigate whether the DTI-NODDI values are biased, Bland-Altman analysis was performed in each dataset (Bland and Altman, 1986). Briefly, Bland-Altman analysis is a method to confirm the presence or absence and degree of systematic bias visually by creating a scatter diagram (Bland-Altman plot), which is created by plotting the difference between two pairs of measured values on the y axis and the average value of the two measured values on the x axis. The reproducibility of each parcel of each estimate was investigated using 32 subjects' test-retest data using the intra-class correlation coefficient (ICC) and the coefficient of reliability (CR) (Bland and Altman, 2003; Shrout and Fleiss, 1979; Vaz et al., 2013). Subsequently, the median value of ICC and CR in all parcels was defined as the representative value of each estimate.

Since the quality of the NODDI estimates depends on the image quality and preprocessing, we estimated the practical quality by the temporal signal-to-noise ratio (tSNR) of preprocessed b=0 volumes and removed surface parcels with tSNR<17 from the analysis. The cutoff was determined

bioRxiv preprint doi: https://doi.org/10.1101/441659; this version posted October 13, 2018. The copyright holder for this preprint (which was not certified by peer review) is the author/funder, who has granted bioRxiv a license to display the preprint in perpetuity. It is made available under aCC-BY-NC-ND 4.0 International license.

empirically in our previous study (Fukutomi et al., 2018).

2.3 *Simulation*

Since correlations and biases between DTI-NODDI and the original NODDI in HCP data were particularly dependent on the presence of high b-value data (b=3000 s/mm$^2$) in the datasets (see section 3.1), simulations were performed to clarify whether potential sources of error can explain our findings of cortical neurite distributions with DTI-NODDI. A potential source of error was the amount of CSF compartment ($V_{iso}$), which was assumed to be zero in the DTI-NODDI model. The size of the CSF compartment in a cortical voxel is the sum of CSF compartment in the cortical tissue and the partial volume of extra-tissue CSF because of the thin cortical ribbon (average 2.6mm, minimum 1.6mm) and the limited spatial resolution of the dMRI data (1.25mm iso-voxel in HCP data) (see also Supplementary text, Fig. S1). The effect of partial voluming may be different across cortical voxels depending on the locations of the voxels within the complex geometry of the cortical ribbon. The various levels of partial volume effects can cause heterogeneity of accuracy in each cortical voxel that could result in errors and biases when mapped on the cortical surface. Particularly, the effect of heterogeneity in CSF partial volume can change the size of the error in DTI-NODDI parameters depending on b-shell scheme of dMRI data, because low b-value dMRI data may contain more CSF signal than high b-value dMRI data. Therefore, it is important to demonstrate the robustness of DTI-NODDI against errors caused by partial voluming of CSF to ensure non-biased distribution of cortical DTI-NODDI maps. Our simulation analyses addressed three potential sources of error. First, the validity of the DTI-NODDI assumption of negligible CSF was evaluated by simulating cerebral cortex that contains a small amount of CSF with little variability (=0.1 in volume ratio). Second, we investigated whether heterogeneity of $V_{iso}$ would cause errors in DTI-NODDI parameters and how the sensitivity of DTI-NODDI to the heterogeneity of $V_{iso}$ error depends on b-shell datasets. Third, random noise in dMRI data was also investigated, because both DTI and the original NODDI model may have biases depending on SNR. Thus, we created simulation data with and without random noise in dMRI and assessed how the noise can affect bias in the measures of DTI-NODDI as compared with the assumed true values from the original NODDI model. All the simulation data were created based on the mathematical equations and derivation described in the Appendix. The details of two simulation analyses including assumed values and conditions are described below.

2.3.1 *Validity of the negligible CSF compartment assumption for cortical DTI-NODDI*

Although we confirmed that CSF volume in the cortex was small (average $V_{iso}$=0.096), it may not be

bioRxiv preprint doi: https://doi.org/10.1101/441659; this version posted October 13, 2018. The copyright holder for this preprint (which was not certified by peer review) is the author/funder, who has granted bioRxiv a license to display the preprint in perpetuity. It is made available under aCC-BY-NC-ND 4.0 International license.

small enough to justify using DTI-NODDI, particularly when using low b-value dMRI data, which might have a significant contribution of CSF. Therefore, we investigated using a simulation analysis whether the value of $V_{iso}$ in the cortex is small enough to use a mathematical relationship between DTI and NODDI that assumes negligible CSF for each b-shell dataset. The size of the CSF compartment ($V_{iso}$) in the cortex was assumed to be homogeneous and small in a simulation analysis ($V_{iso}$=0.1) since our estimated values using original NODDI were 0.096±0.063 (mean ± s.d.) in cortical gray matter and 0.21 ± 0.097 in the white matter (Supplementary Text and Fig. S1). Seven different combinations of b-shell datasets (same as Table 1) were created assuming following parameters as possible values within the cerebral cortex (Fukutomi et al., 2018); $V_{iso}$=0.1, NDI ranging from 0.1 to 0.55 and ODI ranging from 0.040 to 0.84, independently and respectively (see Table 2). To investigate linearity, $NDI_{DTI}$ and $ODI_{DTI}$ were correlated with the true values using the Pearson correlation analysis for each dataset. Subsequently, a Bland-Altman analysis was performed between the original NODDI model and DTI-NODDI to investigate bias in the DTI-NODDI model. In addition, to investigate the effect of random noise in DTI-NODDI, the same analyses were also performed using simulation data with added Gaussian noise to produce a SNR level of 20.

**Table 2**. Parameters and values used in simulation analysis. Note that all combinations of values of NDI and ODI were simulated.

| NDI | 0.1 | 0.15 | 0.2 | 0.25 | 0.3 | 0.35 | 0.4 | 0.45 | 0.5 | 0.55 |
|---|---|---|---|---|---|---|---|---|---|---|
| ODI | 0.040 | 0.11 | 0.16 | 0.30 | 0.37 | 0.47 | 0.55 | 0.61 | 0.70 | 0.84 |

2.3.2 *Error sensitivity of cortical DTI-NODDI to heterogeneity and partial volume effects of CSF*

Although the CSF compartment in the cortex is relatively small as compared with white matter, MRI signal in cortical voxels may have a contribution of CSF by partial volume effects and hence heterogeneity because of the limited resolution of dMRI data (1.25mm iso-voxel in HCP data). To address this, we evaluated the error sensitivity of DTI-NODDI to the heterogeneity of CSF ($V_{iso}$) by systematic simulation with error propagation from $V_{iso}$ to DTI-NODDI parameters. The simulated dMRI datasets were created as cortical gray matter voxels but with different levels of partial volume CSF. The reference parameters were fixed to NDI=0.25, ODI=0.30, and $V_{iso}$=0.1 because they were near the mean values estimated by cortical NODDI. The simulated dMRI datasets were created with different levels of error in $V_{iso}$ at -0.1 (i.e. assumed value of $V_{iso}$=0), 0 (i.e. $V_{iso}$=0.1) and from +0.1 to +0.9 (i.e. $V_{iso}$ from 0.2 to 1.0) with an interval of 0.1. For each simulation dataset, $NDI_{DTI}$ and $ODI_{DTI}$ were calculated by DTI-NODDI, and then, %error in DTI-NODDI was calculated as the ratio of the estimated values to those without error in $V_{iso}$. The same analysis was also performed using

bioRxiv preprint doi: https://doi.org/10.1101/441659; this version posted October 13, 2018. The copyright holder for this preprint (which was not certified by peer review) is the author/funder, who has granted bioRxiv a license to display the preprint in perpetuity. It is made available under aCC-BY-NC-ND 4.0 International license.

simulated data with added Gaussian noise to an SNR level of 20.

## 3. Results

### 3.1 Cortical DTI-NODDI using in vivo dMRI data

#### 3.1.1 *Reliability of DTI-NODDI as compared with the original NODDI*

When the three-shell dataset ($b_{All}$) in 456 subjects of HCP data were used in the original NODDI, the cortical map of neurite density ($NDI_{ORIG}$) showed high intensity in the primary sensorimotor, visual, auditory cortices as well as the middle temporal (MT) area (Fig. 2 A), while $ODI_{ORIG}$ showed high intensity in the primary sensory, visual and auditory areas (Fig. 3 A), as we reported previously (Fukutomi et al., 2018). Moreover, consistent with our previous study (Fukutomi et al., 2018), the cortical distribution of the $NDI_{ORIG}$ was quite similar to that of the myelin map based on the T1w and T2w images, while the distribution of $ODI_{ORIG}$ showed high contrast in the 'granular cortex' of von Economo and Koskinas (von Economo and Koskinas, 1925), where cortical thickness is low and both radial and horizontal fibers are intermingled (Fukutomi et al., 2018).

Interestingly, when DTI-NODDI was applied to the same three-shell dataset ($b_{All}$), similar cortical distributions of NDI and ODI ($NDI_{DTI}$, $ODI_{DTI}$) were obtained in average surface maps across all subjects (Fig. 2 B for $NDI_{DTI}$ and Fig. 3 B for $ODI_{DTI}$). The pattern was also evident in single subject surface maps (Fig. S2 B for $NDI_{DTI}$ and S3 B for $ODI_{DTI}$). The correlation analysis for the parcellated data (see Methods & Materials 2.2.3) showed that correlation coefficients between the DTI-NODDDI and original NODDI were extremely high in group average maps for both metrics (NDI: R=0.97, ODI: R=0.94, $p<0.00001$), as well as individual maps (NDI: R=0.92, ODI: R=0.89, $p<0.00001$) (Fig. 4) although the values were quite different between two methods. The regression equations were as follows; NDI: $Y = 0.81X - 0.11$, ODI: $Y = 1.4X - 0.31$.

bioRxiv preprint doi: https://doi.org/10.1101/441659; this version posted October 13, 2018. The copyright holder for this preprint (which was not certified by peer review) is the author/funder, who has granted bioRxiv a license to display the preprint in perpetuity. It is made available under aCC-BY-NC-ND 4.0 International license.

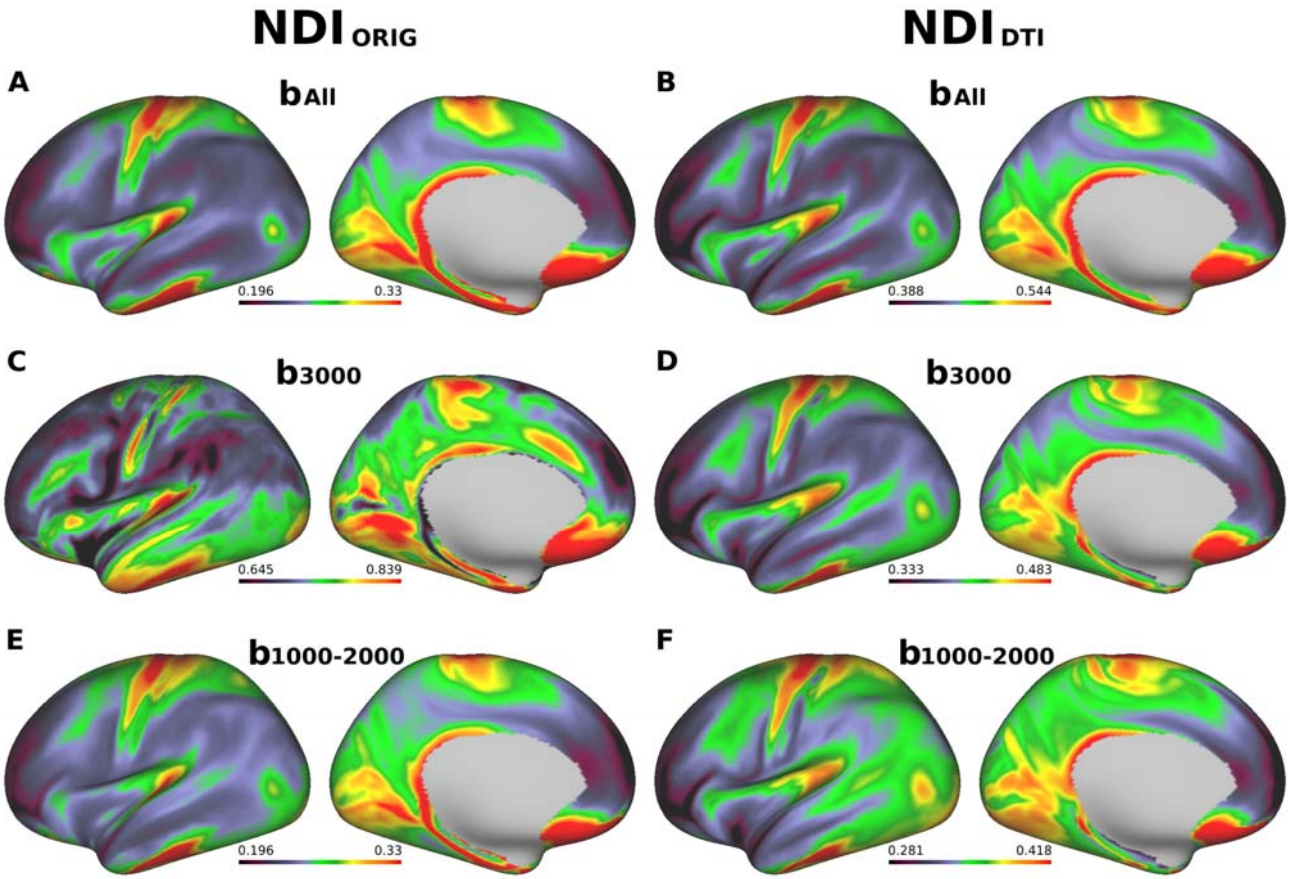


**Figure 2.** Cross-subject average cortical surface maps of neurite density index (NDI). Cortical surfaces are different in terms of computation methods: original NODDI ($NDI_{ORIG}$) vs DTI-NODDI ($NDI_{DTI}$) and b-shell datasets used: all three b-values ($b_{All}$), only those of b=3000 ($b_{3000}$) and two-shell with low b-values ($b_{1000\text{-}2000}$). **A)** Cortical surface maps of NDI calculated using the original NODDI model ($NDI_{ORIG}$) with the three-shell dataset ($b_{All}$), which shows high intensity in primary sensorimotor, visual, auditory cortices as well as the middle temporal (MT) area, as reported previously (Fukutomi et al., 2018). **B)** $NDI_{DTI}$ calculated using the three-shell dataset ($b_{All}$), which shows very similar distributions of contrasts as in A. **C)** $NDI_{ORIG}$ using the one-shell dataset ($b_{3000}$), which shows a different pattern from the reference cortical map in **A**, while $NDI_{DTI}$ using the one-shell high b-value dataset ($b_{3000}$) in **D** shows very similar surface contrasts to the reference in **A**.**E, F**) The cortical neurite maps of two-shell dataset with low b-values ($b_{1000\text{-}2000}$) were also similar to the reference, but not much as those of $b_{All}$ and $b_{3000}$. Data at https://balsa.wustl.edu/xqln

bioRxiv preprint doi: https://doi.org/10.1101/441659; this version posted October 13, 2018. The copyright holder for this preprint (which was not certified by peer review) is the author/funder, who has granted bioRxiv a license to display the preprint in perpetuity. It is made available under aCC-BY-NC-ND 4.0 International license.

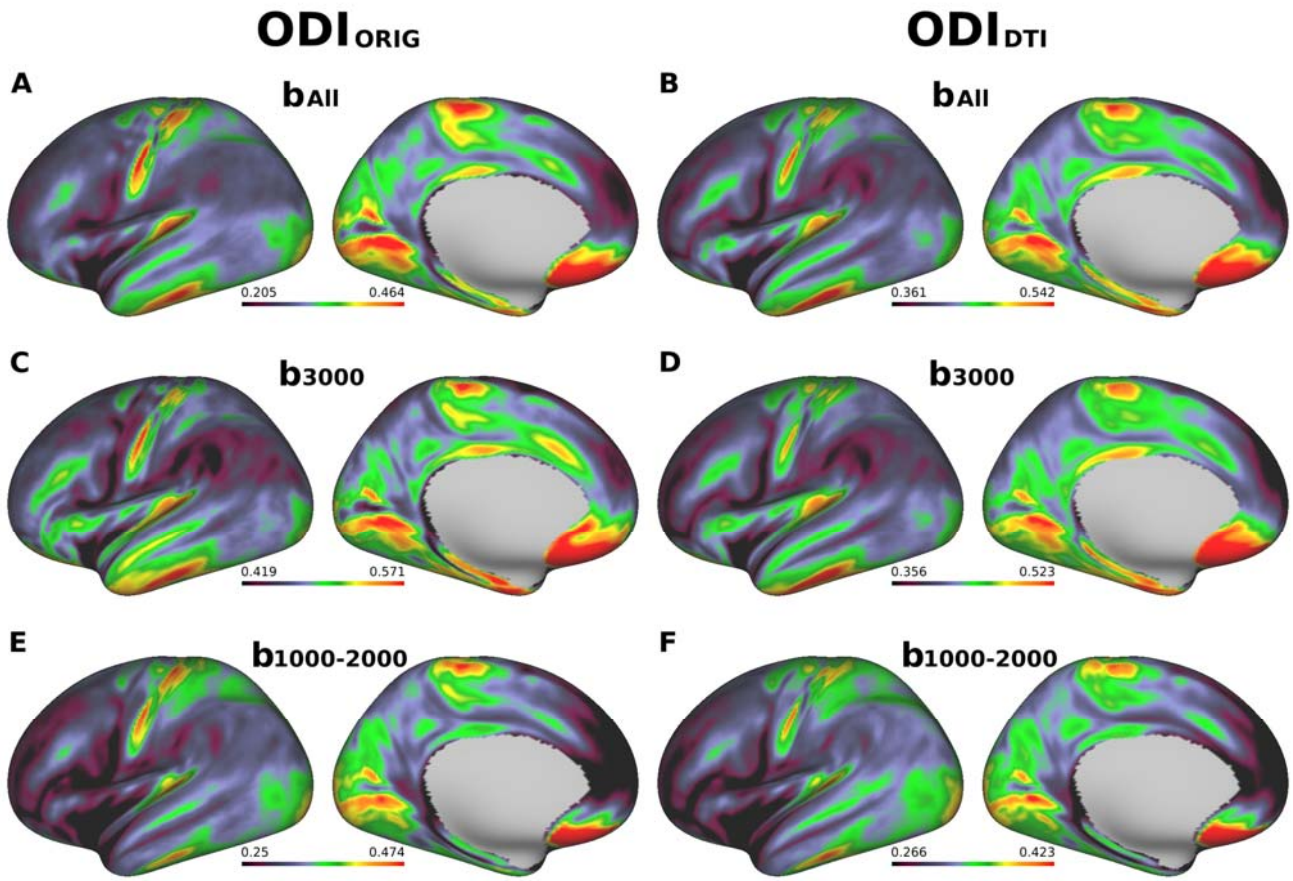


**Figure 3.** Cross-subject average cortical surface maps of orientation dispersion index (ODI). Cortical surfaces are different in terms of computation methods: original NODDI ($ODI_{ORIG}$) vs DTI-NODDI ($ODI_{DTI}$) and the b-shell datasets used: all three b-values ($b_{All}$) vs only those of b=3000 ($b_{3000}$) and two low b-values ($b_{1000-2000}$). **A, C** and **E** show cortical surface maps of ODI calculated using the original NODDI model ($ODI_{ORIG}$) with the three-shell dataset ($b_{All}$), one-shell dataset ($b_{3000}$) and two-shell dataset ($b_{1000-2000}$), respectively. **B, D** and **F** show surface maps of ODI calculated using DTI-NODDI ($ODI_{DTI}$) with the three-shell dataset ($b_{All}$), one-shell high b-value dataset ($b_{3000}$) and two-shell dataset ($b_{1000-2000}$), respectively. Data at https://balsa.wustl.edu/P7LX

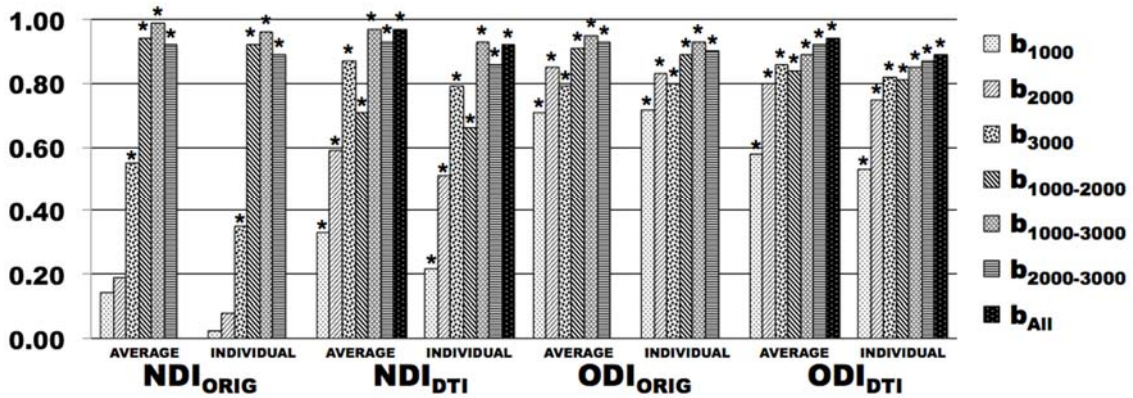


**Figure 4**. Correlation coefficients of NODDI parameters in different calculation methods with those in the reference (NDI_ORIG and ODI_ORIG with b_All). Correlation coefficients were calculated using each b-shell dataset types ($b_{1000}$, $b_{2000}$, $b_{3000}$, $b_{1000-2000}$, $b_{1000-3000}$, $b_{2000-3000}$ and $b_{All}$). Correlation

bioRxiv preprint doi: https://doi.org/10.1101/441659; this version posted October 13, 2018. The copyright holder for this preprint (which was not certified by peer review) is the author/funder, who has granted bioRxiv a license to display the preprint in perpetuity. It is made available under aCC-BY-NC-ND 4.0 International license.

coefficients, which were calculated using average surface maps among all subjects, are shown in "AVERAGE", while average of correlation coefficients, which were calculated in individual subjects, are shown in "INDIVIDUAL". Asterisks (*) denotes statistical significance level with $p<0.00001$. Data at https://balsa.wustl.edu/7MZG

To investigate further this difference of the values between DTI-NODDI and original NODDI parameters, the Bland-Altman analysis was applied to the values of cortical parcellations using those of complete data and original NODDI as a reference. When all of the dMRI data ($b_{All}$) were used, the results of DTI-NODDI showed a consistent bias: $NDI_{DTI}$ overestimated by a difference of around 0.20 and $ODI_{DTI}$ by 0.15 to 0.10 as compared with those of original NODDI (Fig. 5 A, C). Therefore, these findings indicate that despite a steady bias, the DTI-NODDI model allows evaluating variance in cortical neurite properties similar to that in the original NODDI, at least when the full dataset of HCP dMRI was used.

bioRxiv preprint doi: https://doi.org/10.1101/441659; this version posted October 13, 2018. The copyright holder for this preprint (which was not certified by peer review) is the author/funder, who has granted bioRxiv a license to display the preprint in perpetuity. It is made available under aCC-BY-NC-ND 4.0 International license.

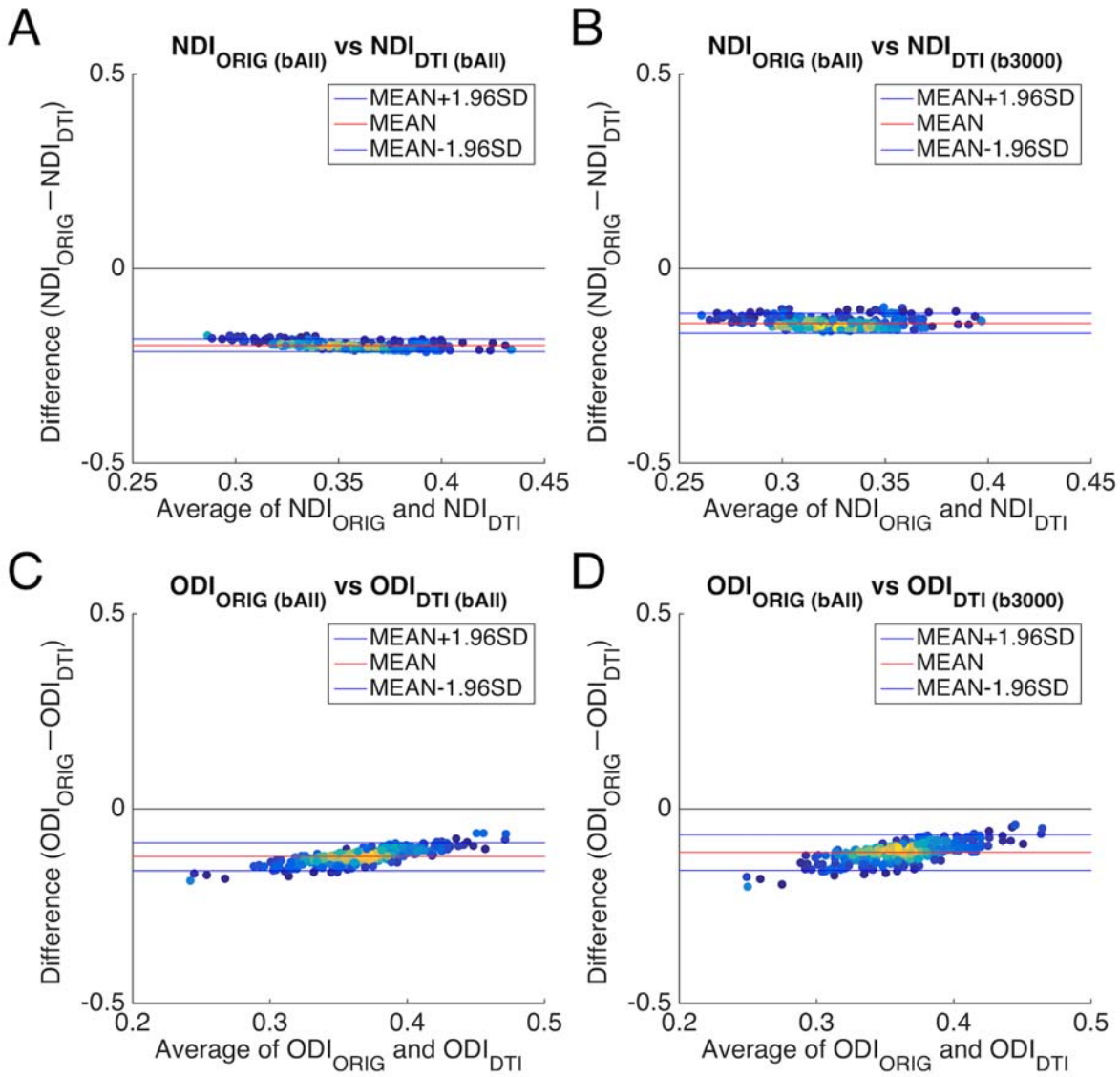


**Figure 5.** Bland-Altman plots between DTI-NODDI and original NODDI in vivo. **A** and **C** show Bland-Altman plots between DTI-NODDI parameters in the three -shell dataset ($b_{All}$) and the original NODDI parameters in the three-shell dataset ($b_{All}$). **B** and **D** show Bland-Altman plots between DTI-NODDI parameters in the high b-value one-shell dataset ($b_{3000}$) and the original NODDI parameters in the three-shell dataset ($b_{All}$). Plots are coloured by their density. Blue lines show the mean±1.96*SD and the red line shows the mean value. Abbreviations; $NDI_{ORIG}$: neurite density index estimated using the original NODDI model, $ODI_{ORIG}$: orientation dispersion index estimated using the original NODDI model, $NDI_{DTI}$: neurite density index estimated using DTI-NODDI, $ODI_{DTI}$: orientation dispersion index estimated using DTI-NODDI. Data at https://balsa.wustl.edu/6gwK

We further tested whether DTI-NODDI can provide valid results given fewer b-shell datasets of dMRI. Interestingly, using a one-shell high b-value dataset ($b_{3000}$), the cortical maps of DTI-NODDI resulted in similar and comparable surface distributions to the reference for both $NDI_{DTI}$ (Fig. 2D)

bioRxiv preprint doi: https://doi.org/10.1101/441659; this version posted October 13, 2018. The copyright holder for this preprint (which was not certified by peer review) is the author/funder, who has granted bioRxiv a license to display the preprint in perpetuity. It is made available under aCC-BY-NC-ND 4.0 International license.

and $ODI_{DTI}$ (Fig. 3D) in average surface maps, while using this one-shell dataset in the original NODDI failed to show such a cortical pattern in NDI (Fig. 2C). The pattern was again evident in a single subject (Fig. S2 D and Fig. S3 D). The correlation coefficients were very high in the group-wise maps for $NDI_{DTI}$ and $ODI_{DTI}$ (R=0.87, R=0.86, respectively, p<0.00001), as well as in individuals (R=0.79, R=0.82, respectively, p<0.00001) (Fig. 4). The regression equations were as follows; NDI: Y = 0.82X - 0.071, ODI: Y = 1.4X - 0.27. The Bland-Altman analysis showed that the high b-value one-shell dataset ($b_{3000}$) had a constant bias of $NDI_{DTI}$ that was a little smaller than that in three-shell dataset ($b_{All}$) (Fig. 5 A, B). The bias of $ODI_{DTI}$ was almost same as in the three-shell dataset (Fig. 5 C, D).

As for the other datasets, a two-shell dataset including a high b-value shell ($b_{1000\text{-}3000}$ and $b_{2000\text{-}3000}$) also provided reasonable and comparable results with the original NODDI surface maps ($NDI_{ORIG}$ and $ODI_{ORIG}$) (Fig. S4 and S5). If b=3000 is included ($b_{1000\text{-}3000}$ sand $b_{2000\text{-}3000}$), both $NDI_{DTI}$ and $ODI_{DTI}$ showed a similar surface distribution to the reference (Fig.S4 A, D, F, Fig.S5 A, D, F). The correlation coefficients were very high in the group-wise maps for both $NDI_{DTI}$ and $ODI_{DTI}$ ($b_{1000\text{-}3000}$: R=0.97, R=0.89, $b_{2000\text{-}3000}$: R=0.93, R=0.92, respectively, p<0.00001), as well as in individuals ($b_{1000\text{-}3000}$: R=0.93, R=0.85, $b_{2000\text{-}3000}$: R=0.86, 0.87, respectively, p<0.00001) (Fig. 4). If a high b-value shell was not included ($b_{1000\text{-}2000}$), which is commonly achievable on clinical 3T scanners, $NDI_{DTI}$ was a little different but still had a similar surface distribution to the reference (Fig. 2 A, F), and the correlation coefficient was reasonably high in the group-wise maps (R=0.71, p<0.00001), as well as in individuals (R=0.66, p<0.00001) (Fig. 4), while $ODI_{DTI}$ showed high correlations in the group-wise maps (R=0.84, p<0.00001), as well as in individuals (R=0.81, p<0.00001) (Fig. 3 A, F, Fig. 4). The Bland-Altman analysis showed that the dataset of high and low b-value two-shell ($b_{1000\text{-}3000}$) (Fig. S6) had a constant bias of $NDI_{DTI}$ and slightly upward sloping bias of $ODI_{DTI}$, which were almost the same size as in the three-shell dataset. High b-value two-shell ($b_{2000\text{-}3000}$) (Fig.S6 A) had also a constant bias of $NDI_{DTI}$ but with a somewhat smaller size than that in three-shell dataset ($b_{All}$). The bias of $ODI_{DTI}$ was almost same size as in the three-shell dataset (Fig. 5 C, S6 B).

One-shell datasets using lower b-value shells (i.e. $b_{1000}$ and $b_{2000}$) did not provide reasonable surface maps of $NDI_{DTI}$ (Fig. S4 L, N) and $ODI_{DTI}$ (Fig. S5 L, N). For example, for the low b-value one-shell dataset ($b_{1000}$), both $NDI_{DTI}$ and $ODI_{DTI}$ showed different surface distributions from the reference (Fig. S4 A, N, Fig. S5 A, N), as well as very low correlation coefficients for $NDI_{DTI}$ (R=0.33 p<0.00001 in group and R=0.22, p<0.00001 in individuals) and $ODI_{DTI}$ (R=0.58, p<0.00001 in group,

bioRxiv preprint doi: https://doi.org/10.1101/441659; this version posted October 13, 2018. The copyright holder for this preprint (which was not certified by peer review) is the author/funder, who has granted bioRxiv a license to display the preprint in perpetuity. It is made available under aCC-BY-NC-ND 4.0 International license.

R=0.53 p<0.00001 in individuals) (Fig. 4). This trend was also found when using the middle high b-value one-shell dataset ($b_{2000}$). Only $ODI_{DTI}$ showed a similar surface distribution to the reference (Fig. S5 A, L) and high correlation coefficients (R=0.80, p<0.00001 in the group average, R=0.75, p<0.00001 in individual) (Fig. 4), while $NDI_{DTI}$ showed different surface distribution from the reference (Fig. S4 A, L) and relatively low correlations (R=0.59, p<0.00001 in the group average, R=0.51, p<0.00001 in individuals) (Fig. 4).

The biases of DTI-NODDI in the other b-shell datasets were shown in Fig. S6. It is of note that although both the three b-shell dataset ($b_{All}$) and one-shell high b-value ($b_{3000}$) had fixed biases of DTI-NODDI, a dataset with low b-value dataset ($b_{1000}$) did not show as large of a bias in the NDI (Fig.S6 A).

It is also of note that the cortical bias dependency on the b-shell scheme was also found in the original NODDI. As described previously, the high b-value one-shell dataset ($b_{3000}$) did not show a comparable cortical distribution of NDI to the reference (Fig. 2C). Other one-shell datasets ($b_{1000}$, $b_{2000}$) in the original NODDI also did not show comparable cortical distribution, particularly in NDI (Fig. S4 A, I, K, M) or high correlations (Fig. 4) with the reference.

As for reproducibility, $NDI_{DTI}$ and $ODI_{DTI}$ showed the highest reproducibility when using the three-shell dMRI data ($b_{All}$) ($NDI_{DTI}$: ICC=0.60, CR=0.0081, $ODI_{DTI}$: ICC=0.64, CR=0.011) among all of datasets (Table S1), followed by datasets with high b-value two-shell ($b_{1000\text{-}3000}$, $b_{2000\text{-}3000}$) and one-shell ($b_{3000}$) (ICC>0.55, CR<0.011) (Table S1). These results did not differ much from those of the original NODDI; e.g. when using three-shell dMRI data ($b_{All}$), $NDI_{ORIG}$: ICC=0.58, CR=0.0073, $ODI_{ORIG}$: ICC=0.64, CR=0.016 (Table S1).

3.1.2 *Calculation time of DTI-NODDI*

The calculation time of the DTI model were less than three minutes per subject using the three-shell dMRI dataset as an input, and that of DTI-NODDI was less than one minute per subject using the DTI model data as the input. Therefore, the total calculation time from dMRI data to the DTI-based NODDI estimates was less than 4 minutes. In contrast, the calculation time of the original NODDI model with AMICO was more than one hour per subject using same computer.

3.2 Results of simulations on the error sources of DTI-NODDI

3.2.1 *Validity of cortical DTI-NODDI to assume negligible CSF*

bioRxiv preprint doi: https://doi.org/10.1101/441659; this version posted October 13, 2018. The copyright holder for this preprint (which was not certified by peer review) is the author/funder, who has granted bioRxiv a license to display the preprint in perpetuity. It is made available under aCC-BY-NC-ND 4.0 International license.

We investigated whether value of $V_{iso}$ (=0.1) in the cortex is small enough to use the mathematical relationship between DTI and NODDI, which assumes negligible CSF for each b-shell dataset using simulation analysis (see 2.3.1 for details). When noise free data were used, $NDI_{DTI}$ and $ODI_{DTI}$ showed extremely strong linear correlation with the ground truth not only in high b-value datasets but also in low b-value datasets (all of them, R>0.97, p<0.00001) (Fig. 6). When Gaussian noise was added, $NDI_{DTI}$ also showed a very strong linear correlation with the ground truth as high as for noise free data in all b-shell datasets. $ODI_{DTI}$ also showed very a strong linear correlation, but somewhat lower than noise free data in all b-shell datasets (Fig. 6).

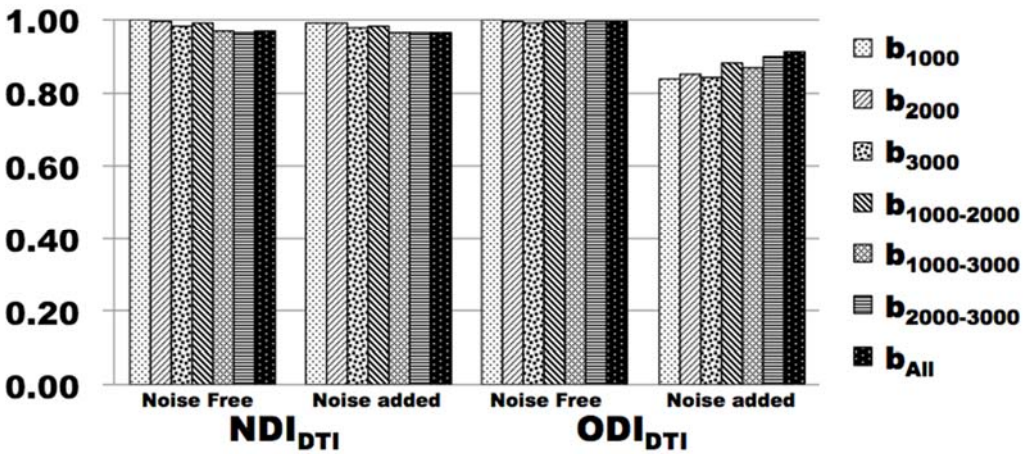


**Figure 6.** Correlation coefficients of DTI-NODDI parameters ($NDI_{DTI}$ and $ODI_{DTI}$) with respect to the ground truth in simulation analysis. Correlation coefficients were calculated using various b-shell dataset types ($b_{1000}$, $b_{2000}$, $b_{3000}$, $b_{1000-2000}$, $b_{1000-3000}$, $b_{2000-3000}$ and $b_{All}$) without noise (Noise Free) and with Gaussian noise such that SNR=20 (Noise Added). All of them have statistical significance level with p<0.00001. Note that this simulation does not consider partial volume effects (see also Figure 7 for simulation of heterogeneity and partial volume effects of CSF). Abbreviations; $NDI_{ORIG}$: neurite density index estimated using the original NODDI model, $ODI_{ORIG}$: orientation dispersion index estimated using the original NODDI model, $NDI_{DTI}$: neurite density index estimated using DTI-NODDI, $ODI_{DTI}$: orientation dispersion index estimated using DTI-NODDI. Data at https://balsa.wustl.edu/17Mg

Despite the high correlation, it is of note that the Bland-Altman analysis showed a constant bias between DTI-NODDI and original NODDI. Both $NDI_{DTI}$ and $ODI_{DTI}$ had a positive constant bias when used with the all b-shell dataset without random noise (Fig. 7 A). The degree of bias was not substantially changed when using high b-value datasets ($b_{3000}$, $b_{1000-3000}$ and $b_{2000-3000}$), but they were smallest or absent when using a dataset of one-shell low b-value (b=1000) (Fig.S7-8). This pattern of bias in $NDI_{DTI}$ and $ODI_{DTI}$ (i.e. constant bias is sensitive to high b-value dMRI data) was basically same when tissue $V_{iso}$ was assumed to be 0 (Fig. S9-10). In addition, the overall patterns of the bias replicated those in HCP data.

bioRxiv preprint doi: https://doi.org/10.1101/441659; this version posted October 13, 2018. The copyright holder for this preprint (which was not certified by peer review) is the author/funder, who has granted bioRxiv a license to display the preprint in perpetuity. It is made available under aCC-BY-NC-ND 4.0 International license.

When the Bland-Altman analysis was performed using the noise added data, the pattern of constant bias in $NDI_{DTI}$ was observed similarly to noise free data (Fig. 7 B), and the slightly upward sloping bias in $ODI_{DTI}$ was observed similarly to in vivo data (Fig. 7 B). These findings in the simulation study suggest that 1) the assumption of negligible $V_{iso}$ in the cortical DTI-NODDI is acceptable at least in terms of the linearity of the values for all types of b-shell datasets. Random noise also slightly degraded estimation of $ODI_{DTI}$, but still the correlation was very high (R>0.8). 2) Since these simulations all assumed that CSF volume of the cortex is 'homogeneously' very low, the next analysis will focus on this issue of inhomogeneity of CSF. 3) There are constant biases of NDI and ODI of DTI-NODDI when high b-value datasets are used. We speculate that these may be due to the error propagation from DTI measures, which are known to be biased when used high b-values dataset (see Discussion 4.3). Actually, our simulation showed that biases of DTI parameters were dependent on the b-values and random noise of data used in the analysis, i.e. when using data with higher b-values, the values of MD were underestimated (Fig. S11) and those of FA were overestimated (Fig. S12). The lower the SNR, the more values of FA were underestimated (Fig. S12), while those of MD were not biased (Fig. S11).

bioRxiv preprint doi: https://doi.org/10.1101/441659; this version posted October 13, 2018. The copyright holder for this preprint (which was not certified by peer review) is the author/funder, who has granted bioRxiv a license to display the preprint in perpetuity. It is made available under aCC-BY-NC-ND 4.0 International license.

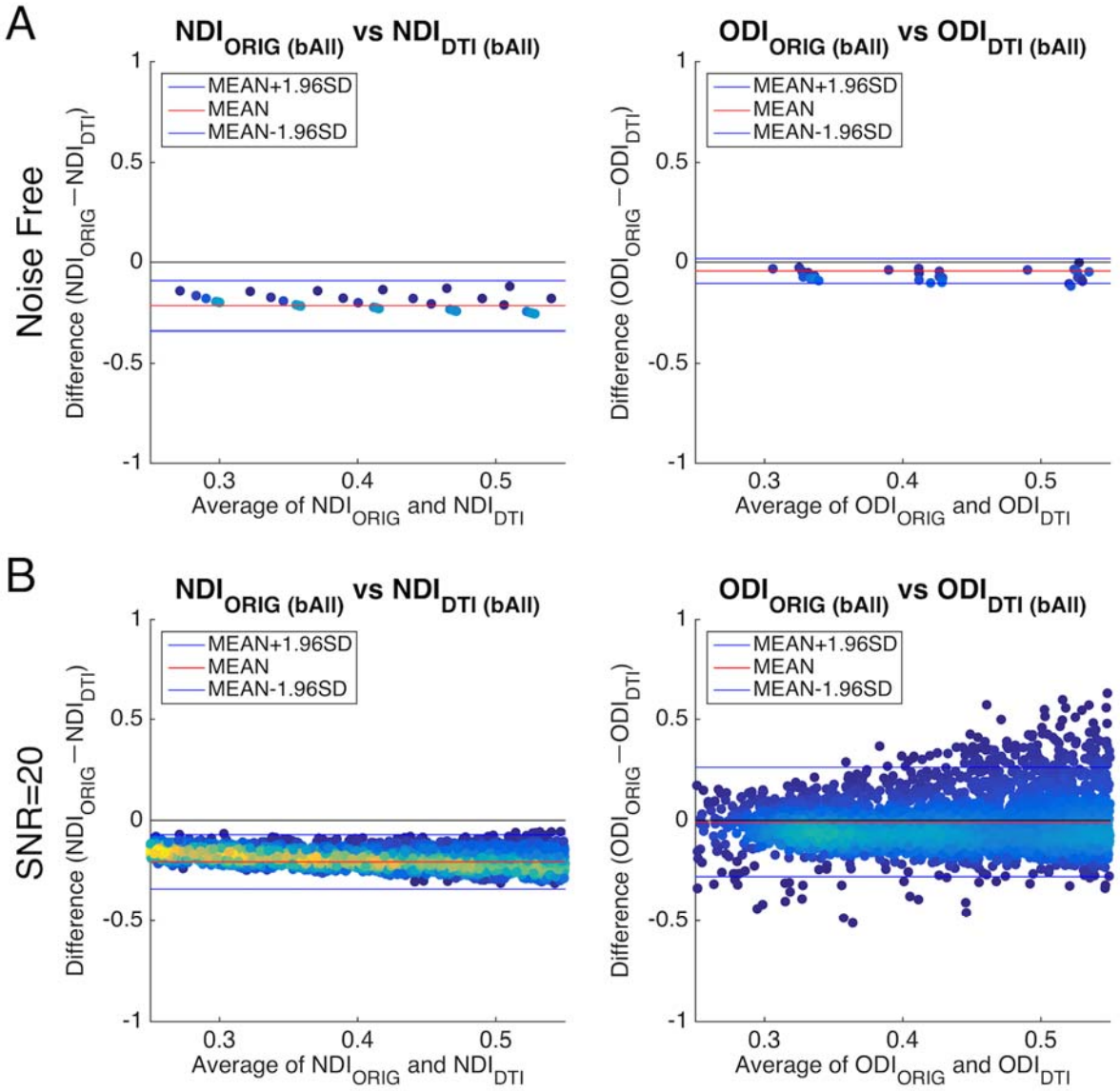


**Figure 7.** Bland-Altman plots between DTI-NODDI parameters and original NODDI parameters using the three-shell dataset (bAll) in simulation analysis. A shows Bland-Altman plots with noise free data. B shows Bland-Altman plots with noise added data such that SNR=20. Plots are coloured by their density. Abbreviations; NDIORIG: neurite density index estimated using the original NODDI model, ODIORIG: orientation dispersion index estimated using the original NODDI model, NDIDTI: neurite density index estimated using DTI-NODDI, ODIDTI: orientation dispersion index estimated using DTI-NODDI. Data at https://balsa.wustl.edu/5njG

3.2.2 *Error sensitivity of cortical DTI-NODDI to heterogeneity and partial volume effects of CSF*

The error sensitivity of DTI-NODDI to heterogeneity of $V_{iso}$ was simulated by analyzing how the errors in DTI-NODDI propagated from the error in $V_{iso}$ (see 2.3.2 for details). By evaluating different b-shell schemes, we found apparent differences in the error sensitivity of DTI-NODDI across different b-shell schemes (Fig. 8). The %error of the DTI-NODDI estimates tended to be

bioRxiv preprint doi: https://doi.org/10.1101/441659; this version posted October 13, 2018. The copyright holder for this preprint (which was not certified by peer review) is the author/funder, who has granted bioRxiv a license to display the preprint in perpetuity. It is made available under aCC-BY-NC-ND 4.0 International license.

smaller in datasets that included high b-value volumes (b=3000) ($b_{3000}$, $b_{1000\text{-}3000}$, $b_{2000\text{-}3000}$ and $b_{All}$) than in those not including b=3000 images ($b_{1000}$, $b_{2000}$, and $b_{1000\text{-}2000}$) when noise level was SNR=20 (Fig. 8A); i.e. b-shell datasets including b=3000 images were more robust against heterogeneity of $V_{iso}$ than low b-value datasets. The largest %error in $NDI_{DTI}$ and $ODI_{DTI}$ were found in low b-value one-shell dMRI data ($b_{1000}$) and the smallest %error were found in the three-shell dMRI data ($b_{All}$), with similar %error in high b-value two-shell dMRI data ($b_{1000\text{-}3000}$). Random noise levels also affected the degree of %errors but did not change the ranking of b-shell datasets (Fig. 8B). These differences in the error sensitivity of $V_{iso}$ should be a major contributor of the difference in linearity among different b-shell datasets.

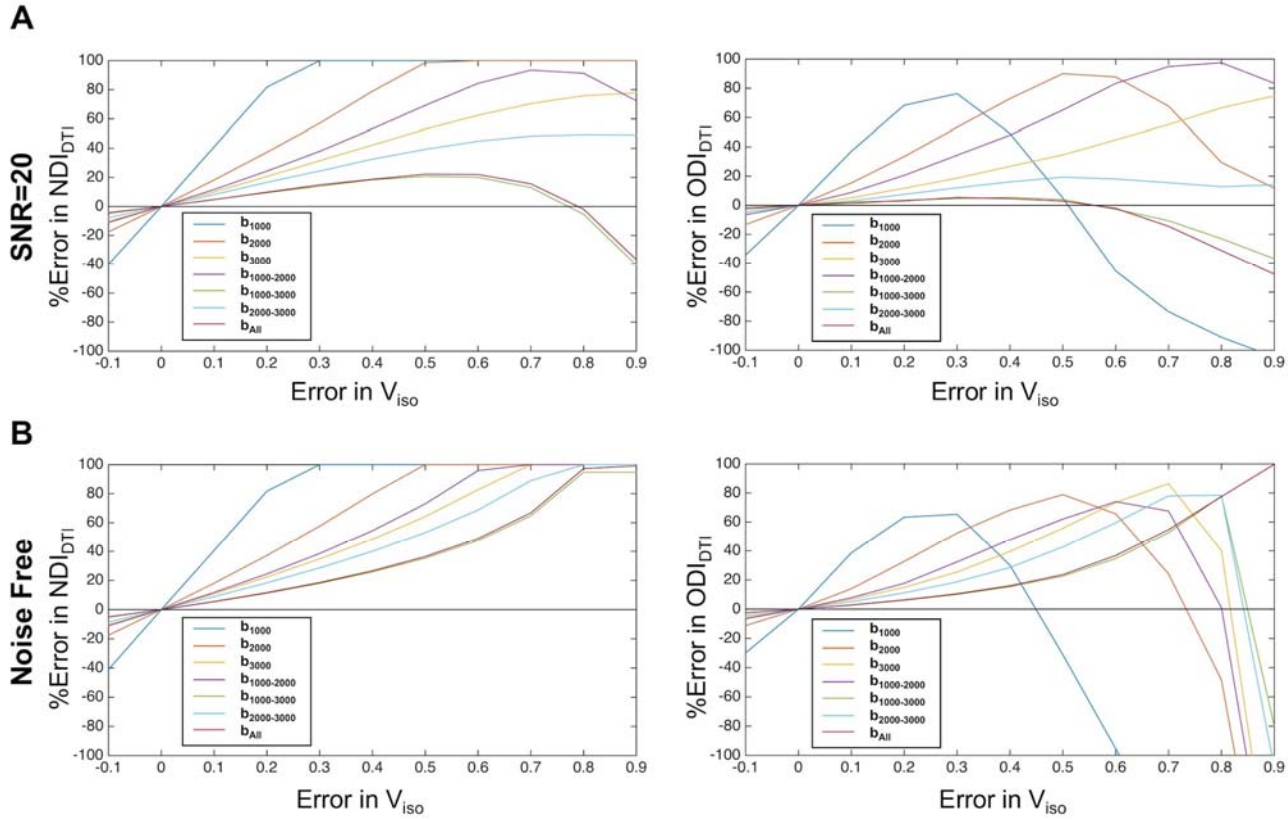


**Figure 8.** Error propagation of the DTI-NODDI from error in the CSF volume fraction ($V_{iso}$). The %error in the estimate of DTI-NODDI was simulated under variable errors in $V_{iso}$ relative to a true value ($V_{iso}$=0.1). **A)** Results when using noise-added datasets with a noise level of SNR=20, **B)** Results when using noise-free datasets. Dataset types of b-shell schemes $b_{1000}$, $b_{2000}$, $b_{3000}$, $b_{1000\text{-}2000}$, $b_{1000\text{-}3000}$, $b_{2000\text{-}3000}$ and $b_{All}$ are shown in different colored lines as in the legend in each graph. Note that the one-shell low b-value data set ($b_{1000}$) is the largest error among all the datasets and particularly sensitive to small error in $V_{iso}$, which may include partial volume effects in the cortical gray matter. The smallest error was found when using the three-shell dMRI data (bAll) or the high b-value two-shell dMRI data (b1000-3000). Abbreviations; $NDI_{DTI}$: neurite density index estimated using DTI-NODDI, $ODI_{DTI}$: orientation dispersion index estimated using DTI-NODDI, SNR: signal noise ratio. Data at https://balsa.wustl.edu/nPxP

bioRxiv preprint doi: https://doi.org/10.1101/441659; this version posted October 13, 2018. The copyright holder for this preprint (which was not certified by peer review) is the author/funder, who has granted bioRxiv a license to display the preprint in perpetuity. It is made available under aCC-BY-NC-ND 4.0 International license.

## Discussion

We found that cortical DTI-NODDI showed a high correlation with known cortical distributions of neurite properties of the original NODDI, particularly when using high b-value dMRI data. The similarity was also evident even when one-shell high b-value dMRI data was used for DTI-NODDI. The amount of CSF estimated in the cerebral cortex using the original NODDI was small but non-zero. The simulation study revealed less sensitivity of errors in DTI-NODDI to partial voluming and heterogeneity of CSF particularly when using high b-value dMRI data. However, the HCP data and simulation showed that high b-value dMRI data resulted in a constant numerical bias, i.e. same amount of error over the range of values.

The mathematical solution of DTI-NODDI indicated one-to-one correspondence between DTI-MD and NODDI-NDI over an expected range of values (Fig. 1). The NODDI NDI is an inverse function of DTI MD as shown in Eq. (2) and Fig. 1A, while the NODDI ODI is a function of both DTI FA and MD as in Eq. (3)-(5) and Fig. 1B. The former relationship was in fact confirmed by in vivo data in human brain (Fukutomi et al., 2018), which showed high correlation between cortical DTI MD and NODDI NDI (R=0.97) as in Fig. 4 B (Fukutomi et al., 2018). However, this observation was based on the measures calculated using the all b-value dataset of HCP (b=1000, 2000, 3000), and the relationship between ODI and DTI measures was not explored. Therefore, the present study extensively studied the validity of the DTI-NODDI using different dMRI b-value schemes in the same HCP subjects.

Our simulations indicated that in any b-shell scheme the DTI-NODDI has a reasonably close relationship to the original NODDI even when noise is added (Fig. 6), while the in vivo measures of cortical DTI-NODDI agreed only when using datasets that included the high b-value shell (b=3000) (Fig. 4). When not using the high b-value shell, the cortical distribution of NDI and ODI of DTI-NODDI showed completely different pattern from those of original NODDI (Fig. S4-5). Why was the predictability of DTI-NODDI degraded when not using high b-value data, and why did the low b-value DTI-NODDI show poor correlation in spatial pattern? Our simulation suggests this is because low b-value DTI-NODDI is more sensitive to errors due to heterogeneity and partial voluming of CSF (Fig. 8). Low b-value dMRI is theoretically sensitive to fluid signals or 'T2 shine-through' effect as well as to tissue diffusivity, whereas high b-value dMRI is more specific to tissue diffusivity (Burdette et al., 2001; DeLano et al., 2000). In addition, the partial volume effects of CSF may vary across cortical regions according to cortical thickness and their heterogeneity within the cortex is an important and unavoidable issue when using currently available MRI

bioRxiv preprint doi: https://doi.org/10.1101/441659; this version posted October 13, 2018. The copyright holder for this preprint (which was not certified by peer review) is the author/funder, who has granted bioRxiv a license to display the preprint in perpetuity. It is made available under aCC-BY-NC-ND 4.0 International license.

(Gonzalezballester, 2002). The DTI model also suffers from a partial volume effect of CSF and results in fitting error particularly in the cortex (Basser et al., 1994b; Papadakis et al., 1999), as it does not consider a CSF compartment explicitly like in NODDI. Although the partial volume effect is reduced by surface-based analysis reduces compared to volume-based analysis (see Supplementary text, Fig. S1), it is not completely removed.

Despite the high correlation of cortical metrics with original NODDI, the numerical values of DTI-NODDI when using high b-value data were not the same as those in the original NODDI. Bland-Altman plots of DTI-NODDI in HCP data showed a positive fixed bias in both NDI and ODI, particularly when using datasets with high b-value (b=3000), and the bias was the least when used a single-shell dataset of low b-value (b=1000) (Fig. 5, S6-7). This pattern was also confirmed in the simulation study, in which positive bias was the largest in DTI-NODDI using the high b-value datasets and the least when using the low b-value dataset, regardless of tissue CSF or random noise (Fig. 7, Fig.S7-8 and Fig. S9-10). The biases of DTI-NODDI are likely caused by the biases already in DTI, since measures of the former are mathematically calculated from those of the latter (Fig. 1). In fact, our full simulation showed that biases of DTI parameters were dependent on the b-values of data and random noise of data used in the analysis, i.e. when using data with higher b-values, the values of MD were underestimated (Fig. S11) and those of FA were overestimated (Fig. S12). The lower the SNR, the more values of FA were underestimated (Fig. S12), whereas those of MD were not biased (Fig. S11). These results were also consistent with previous studies, e.g. MD is biased to lower value by using dMRI data with higher b-value than with standard b-value (b=1000) (Hui et al., 2010), and FA is positively biased with lower SNR, while MD is robust to lower SNR (Farrell et al., 2007; Jones and Basser, 2004; Pierpaoli and Basser, 1996). Therefore, according to Eq (3)-(5), using low SNR data may enhance the positive bias in FA and hence cause an upward bias in $ODI_{DTI}$. Therefore, the fixed biases of DTI-NODDI comes from the DTI model and non-linearity of the actual data, rather than the partial volume effect of CSF. Edwards et al. also refer to the kurtosis of diffusion signals in high b-value data, which can cause the bias in the DTI-NODDI (Edwards et al., 2017).

The current study shows a potential use of DTI-NODDI in estimating cortical neurites, however, there are many caveats when practically using this. One advantage of cortical DTI-NODDI may be that it could allow shorter dMRI scans, which could be helpful for clinical studies such as Alzheimer's disease. DTI can be estimated with relatively few directions - at least 6 or in general more than 30 are recommended (Jones, 2004), whereas the original NODDI is recommended with at

bioRxiv preprint doi: https://doi.org/10.1101/441659; this version posted October 13, 2018. The copyright holder for this preprint (which was not certified by peer review) is the author/funder, who has granted bioRxiv a license to display the preprint in perpetuity. It is made available under aCC-BY-NC-ND 4.0 International license.

least 90 directions (Zhang et al., 2012). Even scanning with high spatial resolution dMRI as in the HCP, the duration of a dMRI scan with 30 directions should not exceed 3 min. On the other hand, there are several disadvantages of using DTI-NODDI. First, when scanning with high b-values, it is uncertain whether the bias due to kurtosis will be near-constant even in pathological brains. Thus, this needs to be addressed in clinical studies to evaluate homogeneous sensitivity to cortical pathologies. There is also a possible improvement in the accuracy of cortical DTI-NODDI by applying a special sequence, such as 'fluid-attenuated inversed recovery DTI', reducing CSF signal in tissue even in low b-value dMRI (Chou et al., 2005; Kwong et al., 1991), potentially allowing low b-value DTI-NODDI without partial voluming of CSF. Second, the limited number of directions of dMRI may hamper sophisticated analysis such as diffusion tractography that usually requires high number of directions. Therefore, short time dMRI data optimized for DTI-NODDI could not be used for such a sophisticated analysis.

Additional issues remain to be discussed. First, there is debate over the optimality of NODDI. Two issues will be discussed here as they relate to the current study. 1) In the current study, we considered the original NODDI parameters calculated using the three-shell dMRI datasets to be a 'gold standard', however, the optimal b-shell scheme for NODDI for true neurite estimation is still an open question. The original study that proposed NODDI suggested that the values of NODDI parameters did not strongly differ as long as two b-shell datasets were used (Zhang et al., 2012). This was consistent with the present study, which showed that in any combinations of two-shell datasets, the original NODDI measures were strongly correlated with those of the 'gold standard' three-shell dataset (Fig. 4). The optimal b-shell scheme of NODDI is, however, difficult to determine and out of scope of the current study, as in general the accuracy of non-linear fitting of the model largely relies on the number of discrete datasets, which is practically limited to a small number of b-shells in clinical dMRI. Therefore, we used the full three-shell dataset in HCP as a gold-standard of NODDI parameters. 2) The second issue is related to the assumptions of intrinsic diffusivity in the original NODDI model, which is also applicable to DTI-NODDI. Recent studies showed that the intrinsic diffusivity in the tortuosity model used in NODDI may not be realistic, and different between in the intra- and extra-neurite compartments (Jelescu et al., 2016), and the value of intrinsic diffusivity is variable across brain regions (Kaden et al., 2016). However, they needed to ignore the CSF compartment to estimate variability of the intrinsic diffusivity. There is also a recent attempt to apply a diffusion model using a general framework without fixing diffusivity (Lampinen et al., 2017), though stability, robustness, histological validity need to be evaluated.

bioRxiv preprint doi: https://doi.org/10.1101/441659; this version posted October 13, 2018. The copyright holder for this preprint (which was not certified by peer review) is the author/funder, who has granted bioRxiv a license to display the preprint in perpetuity. It is made available under aCC-BY-NC-ND 4.0 International license.

Second, the current technique of DTI-NODDI needs to be carefully extended for application. As discussed above, the current analysis is all based on the data of young healthy subjects in HCP, and it is premature to conclude that DTI-NODDI can also provide similar results to NODDI in clinical patients. Thus further investigations are needed in the future. The technique also needs to be tested for investigating the neurite properties in the white matter. In fact, Edwards et al. applied DTI-NODDI in the white matter using one-shell low b-value dMRI data (Edwards et al., 2017) and they applied a correction of the bias due to kurtosis.

## 5. Conclusion

Cortical DTI-NODDI showed similar distributions to that of the original NODDI model, particularly when using at least one-shell of high b-value dMRI data. The DTI-NODDI with low b-value dMRI should have a smaller bias in absolute quantity in simulation but is practically biased in in vivo cortical distribution due to heterogeneity and partial voluming of CSF. These findings suggest that DTI can predict microstructural features related to neurites in the cerebral cortex at least when the conditions of data acquisition meet certain requirements such as a high b-value shell and high spatial resolution of dMRI.

## 6. Notes

Data of Supplementary Figures are available at https://balsa.wustl.edu/7M1q

## 7. Acknowledgements

All authors declare no conflict of interest. The data of this study were provided by the Human Connectome Project, WU-Minn Consortium (Principal Investigators: David Van Essen and Kamil Ugurbil; 1U54MH091657) funded by the 16 NIH Institutes and Centers that support the NIH Blueprint for Neuroscience Research; and by the McDonnell Center for Systems Neuroscience at Washington University. This research is partially supported by the program for Brain Mapping by Integrated Neurotechnologies for Disease Studies (Brain/MINDS) and Brain/MINDS-beyond from Japan Agency for Medical Research and development, AMED (JP18dm0207001, JP18dm0307006), by RIKEN Compass to Healthy Life Research Complex Program from Japan Science and Technology Agency, JST, by MEXT KAKENHI Grant (16H03300, 16H03306) (T.H.).

bioRxiv preprint doi: https://doi.org/10.1101/441659; this version posted October 13, 2018. The copyright holder for this preprint (which was not certified by peer review) is the author/funder, who has granted bioRxiv a license to display the preprint in perpetuity. It is made available under aCC-BY-NC-ND 4.0 International license.

## 8. Appendix

In this section, we described formulation and derivation of the NODDI model, by which simulation study was performed. In the NODDI model, the signal ($A$) of the tissue is composed of CSF ($A_{iso}$), extracellular ($A_{ec}$) and intracellular compartments ($A_{ic}$) (Zhang et al., 2012) as in Eq. 1. The signal is also dependent on volume fractions of the CSF compartment ($\nu_{iso}$.) and the intracellular compartments ($\nu_{ic}$). We describe in detail how each of $A_{iso}$, $A_{ec}$, and $A_{ic}$ can be expressed mathematically. We also describe how the Watson distribution can be expressed by a mathematical equation.

1. CSF compartment ($A_{iso}$)

Since $A_{iso}$ is dependent on isotropic diffusion, it can be expressed as

$$A_{iso} = e^{-bd_{iso}}, \tag{A1}$$

where $b$ is b-value of dMRI and $d_{iso}$ is the diffusion coefficient of the CSF.

2. Extracellular compartment ($A_{ec}$)

According to Zhang et al. (Zhang et al., 2012), $A_{ec}$ is expressed as follows:

$$A_{ec} = \exp\left(-b\boldsymbol{q}^T \cdot \int_{\mathbb{S}^2} f(\boldsymbol{n}|\boldsymbol{\mu},\kappa)D(\boldsymbol{n})\, d\boldsymbol{n} \cdot \boldsymbol{q}\right), \tag{A2}$$

where $\boldsymbol{q}$ is an unit vector which is the direction of diffusion weighting gradient and $D(\boldsymbol{n})$ is a cylindrical symmetry tensor whose main axis is along the direction of $\boldsymbol{n}$.

On the other hand, according to Zhang et al. (Zhang et al., 2012), let $d_{\parallel}$ and $d_{\perp}$ be the diffusion coefficients which are parallel and perpendicular to the main axis in the intracellular compartment, respectively. The diffusion coefficients ($d'_{\parallel}$ and $d'_{\perp}$) which are parallel and perpendicular to the main axis in the extracellular compartment, are expressed as follows:

$$\begin{cases} d'_{\parallel} = d_{\parallel} - d_{\parallel}\nu_{ic}(1-\tau_1) \\ d'_{\perp} = d_{\parallel} - d_{\parallel}\nu_{ic}\left(\dfrac{1+\tau_1}{2}\right), \end{cases} \tag{A3}$$

where $\tau_1$ is expressed as follows (Zhang et al., 2012):

$$\tau_1 = -\frac{1}{2\kappa} + \frac{1}{\sqrt{\pi\kappa}\cdot e^{-\kappa}\cdot erfi(\sqrt{\kappa})}, \tag{A4}$$

where $erfi(x)$ is the incomplete error function and given as below:

bioRxiv preprint doi: https://doi.org/10.1101/441659; this version posted October 13, 2018. The copyright holder for this preprint (which was not certified by peer review) is the author/funder, who has granted bioRxiv a license to display the preprint in perpetuity. It is made available under aCC-BY-NC-ND 4.0 International license.

$$erfi(x) = \frac{2}{\sqrt{\pi}} \int_0^x e^{t^2} dt. \tag{A5}$$

Since the principal axis of the extracellular compartment is assumed to be parallel to the z-axis, $\boldsymbol{D_{ec}}(\hat{\boldsymbol{z}}, \kappa)$ is expressed as below:

$$\boldsymbol{D_{ec}}(\hat{\boldsymbol{z}}, \kappa) = \begin{pmatrix} d'_{\perp} & 0 & 0 \\ 0 & d'_{\perp} & 0 \\ 0 & 0 & d'_{\parallel} \end{pmatrix}. \tag{A6}$$

Therefore, $A_{ec}$ is rewritten using Eq. (A2), (A6) as below:

$$A_{ec} = exp(-b\boldsymbol{q}^T \cdot \boldsymbol{D_{ec}}(\boldsymbol{\mu}, \kappa) \cdot \boldsymbol{q}) . \tag{A7}$$

Since $\boldsymbol{D_{ec}}(\boldsymbol{\mu}, \kappa)$ is a cylindrically symmetric tensor whose principal axis is in the direction of the principal axis of the Watson distribution (described in detail Appendix 4), namely $\boldsymbol{\mu}$, $\boldsymbol{q}^T \cdot \boldsymbol{D_{ec}}(\boldsymbol{\mu}, \kappa)\boldsymbol{q}$ is a function of $\theta = \boldsymbol{q} \cdot \boldsymbol{\mu}$ which is the relative angle between the principal axes of MPG and Watson distribution. Hence, without loss of generality, let $\boldsymbol{\mu} = \hat{\boldsymbol{z}}$. Since $\boldsymbol{D_{ec}}(\hat{\boldsymbol{z}}, \kappa)$ is cylindrically symmetrical to the z-axis in this case, $A_{ec}$ depends only on $\theta = \boldsymbol{q} \cdot \boldsymbol{\mu}$, which is the angle between MPG and z-axis, not on the azimuthal angle $\phi$. Hence, without loss of generality, let $\phi = 0$. Now, let $\boldsymbol{R}(-\theta_{\boldsymbol{q}})$ be the rotation matrix, which makes the direction of MPG ($\boldsymbol{q}$) parallel to z-axis,

$$\begin{aligned} \boldsymbol{q}^T \cdot \boldsymbol{D_{ec}}(\hat{\boldsymbol{z}}, \kappa)\boldsymbol{q} &= \left(\boldsymbol{R}(-\theta_{\boldsymbol{q}}) \cdot \boldsymbol{q}\right)^T \cdot \boldsymbol{D_{ec}}\left(\boldsymbol{R}(-\theta_{\boldsymbol{q}}) \cdot \hat{\boldsymbol{z}}, \kappa\right) \cdot \left(\boldsymbol{R}(-\theta_{\boldsymbol{q}}) \cdot \boldsymbol{q}\right) \\ &= \hat{\boldsymbol{z}}^T \cdot \boldsymbol{D_{ec}}\left(\boldsymbol{R}(-\theta_{\boldsymbol{q}}) \cdot \hat{\boldsymbol{z}}, \kappa\right) \cdot \hat{\boldsymbol{z}} \\ &= (0 \quad 0 \quad 1) \begin{pmatrix} 1 & 0 & 0 \\ 0 & cos\theta & -sin\theta \\ 0 & sin\theta & cos\theta \end{pmatrix}^T \begin{pmatrix} d'_{\perp} & 0 & 0 \\ 0 & d'_{\perp} & 0 \\ 0 & 0 & d'_{\parallel} \end{pmatrix} \begin{pmatrix} 1 & 0 & 0 \\ 0 & cos\theta & -sin\theta \\ 0 & sin\theta & cos\theta \end{pmatrix} \begin{pmatrix} 0 \\ 0 \\ 1 \end{pmatrix} \\ &= d'_{\perp} sin^2\theta + d'_{\perp} cos^2\theta. \end{aligned} \tag{A8}$$

Summarizing the above, $A_{ec}$ is denoted using Eq. (A7), (A8) as below:

$$A_{ec} = exp\left(-b(d'_{\perp} sin^2\theta + d'_{\perp} cos^2\theta)\right), \tag{A9}$$

where $\theta = \boldsymbol{q} \cdot \boldsymbol{\mu}$.

3. Intracellular compartment ($A_{ic}$)

According to Zhang et al.,

bioRxiv preprint doi: https://doi.org/10.1101/441659; this version posted October 13, 2018. The copyright holder for this preprint (which was not certified by peer review) is the author/funder, who has granted bioRxiv a license to display the preprint in perpetuity. It is made available under aCC-BY-NC-ND 4.0 International license.

$$A_{ic} = \int_{\mathbb{S}^2} f(\boldsymbol{n}|\boldsymbol{\mu},\kappa) e^{-bd_{\parallel}(\boldsymbol{q}\cdot\boldsymbol{n})^2}\, d\boldsymbol{n}\,, \tag{A10}$$

where $d_{\parallel}$ is intrinsic diffusivity. $A_{ic}$ cannot be expressed by elementary functions. First, the Watson distribution is expanded using spherical harmonics. Let $f_{l0}^{c}(\kappa)$ be an expansion coefficient, when $f(\boldsymbol{n}|\hat{\boldsymbol{z}},\kappa)$ is expanded using spherical harmonics.

$$f(\boldsymbol{n}|\hat{\boldsymbol{z}},\kappa) = \sum_{l=0}^{\infty} f_{l0}^{c}(\kappa) Y_{l0}(\theta_{\boldsymbol{n}},0). \tag{A11}$$

The Watson distribution $f(\boldsymbol{n}|\boldsymbol{\mu},\kappa)$, whose mean orientation is $\boldsymbol{\mu}$, is expressed by using Wigner Rotation Matrix (A Morrison and A Parker, 1987) as follows:

$$\begin{aligned}
f(\boldsymbol{n}|\boldsymbol{\mu},\kappa) &= f\left(\boldsymbol{n}|\mathbf{R}\left(-\theta_{\mathbf{q}}\right)\hat{\boldsymbol{z}},\kappa\right) \\
&= \mathbf{R}\left(\theta_{\mathbf{q}}\right) f(\boldsymbol{n}|\hat{\boldsymbol{z}},\kappa) \\
&= \mathbf{R}(\theta_{\mathbf{q}}) \sum_{l=0}^{\infty} f_{l0}^{c}(\kappa) Y_{l0}(\theta_{\boldsymbol{n}},0) \\
&= \sum_{l=0}^{\infty} f_{l0}^{c}(\kappa) \mathbf{R}(\theta_{\mathbf{q}}) Y_{l0}(\theta_{\boldsymbol{n}},0) \\
&= \sum_{l=0}^{\infty} f_{l0}^{c}(\kappa) \sum_{m'=-l}^{l} Y_{lm'}(\theta_{\boldsymbol{n}},\phi_{\boldsymbol{n}}) \sqrt{\frac{4\pi}{2l+1}} Y_{lm'}^{*}(\theta_{\boldsymbol{q}},0),
\end{aligned} \tag{A12}$$

where $\theta_{\boldsymbol{q}}$ is the angle between MPG direction and z-axis.

We substitute this into the $A_{ic}$ (at this time $\mathbf{q} = \hat{\mathbf{z}}$), because if $\mathrm{m} \neq 0$, $\int_0^{2\pi} e^{im\phi}\, d\phi = 0$, and if $\mathrm{m} = 0, \int_0^{2\pi} 1\, d\phi = 2\pi$.

$$\begin{aligned}
A_{ic} &= \int_{\mathbb{S}^2} \sum_{l=0}^{\infty} f_{l0}^{c}(\kappa) \sum_{m'=-l}^{l} Y_{lm'}(\theta_{\boldsymbol{n}},\phi_{\boldsymbol{n}}) \sqrt{\frac{4\pi}{2l+1}} Y_{lm'}^{*}(\theta_{\boldsymbol{q}},0) e^{-bd_{\parallel}(\hat{\boldsymbol{z}}\cdot\boldsymbol{n})^2}\, d\boldsymbol{n} \\
&= \int_{\mathbb{S}^2} \sum_{l=0}^{\infty} f_{l0}^{c}(\kappa) \sum_{m'=-l}^{l} Y_{lm'}(\theta_{\boldsymbol{n}},\phi_{\boldsymbol{n}}) \sqrt{\frac{4\pi}{2l+1}} Y_{lm'}^{*}(\theta_{\boldsymbol{n}},0) e^{-bd_{\parallel}(\hat{\boldsymbol{z}}\cdot\boldsymbol{n})^2}\, d\boldsymbol{n} \\
&= \sum_{l=0}^{\infty} f_{l0}^{c}(\kappa) \sum_{m'=-l}^{l} \sqrt{\frac{4\pi}{2l+1}} Y_{lm'}^{*}(\theta_{\boldsymbol{q}},0) \int_0^{2\pi} sin\theta_{\boldsymbol{n}} d\phi_{\boldsymbol{n}} \int_0^{\pi} d\theta_{\boldsymbol{n}}\, Y_{lm'}(\theta_{\boldsymbol{n}},\phi_{\boldsymbol{n}}) e^{-bd_{\parallel}cos^2\theta_{\boldsymbol{n}}} \\
&= \sum_{l=0}^{\infty} f_{l0}^{c}(\kappa) \sum_{m'=-l}^{l} \sqrt{\frac{4\pi}{2l+1}} Y_{lm'}^{*}(\theta_{\boldsymbol{q}},0) \int_0^{2\pi} sin\theta_{\boldsymbol{n}} d\phi_{\boldsymbol{n}} \int_0^{\pi} d\theta_{\boldsymbol{n}} \sqrt{\frac{2l+1}{4\pi}\frac{(l-m')!}{(l+m')!}} P_l^{m'}(cos\theta_{\boldsymbol{n}}) e^{im'\phi_{\boldsymbol{n}}} e^{-bd_{\parallel}cos^2\theta_{\boldsymbol{n}}} \\
&= \sum_{l=0}^{\infty} f_{l0}^{c}(\kappa) \sqrt{\frac{4\pi}{2l+1}} Y_{l0}^{*}(\theta_{\boldsymbol{q}},0) 2\pi \int_{-1}^{1} dx \sqrt{\frac{2l+1}{4\pi}} P_l(x) e^{-bd_{\parallel}x^2}
\end{aligned}$$

bioRxiv preprint doi: https://doi.org/10.1101/441659; this version posted October 13, 2018. The copyright holder for this preprint (which was not certified by peer review) is the author/funder, who has granted bioRxiv a license to display the preprint in perpetuity. It is made available under aCC-BY-NC-ND 4.0 International license.

$$= 2\pi \sum_{l=0}^{\infty} f_{l0}^{c}(\kappa) \sqrt{\frac{2l+1}{4\pi}} P_l(cos\theta_{\boldsymbol{q}}) \int_{-1}^{1} dx\, P_l(x) e^{-bd_{\parallel}x^2} \qquad (A13)$$

On the other hand, $f_{l0}^{c}(\kappa)$ are expansion coefficients, when $f(\boldsymbol{n}|\hat{\boldsymbol{z}},\kappa)$ is expressed using spherical harmonics.

$$f(\boldsymbol{n}|\hat{\boldsymbol{z}},\kappa) = \sum_{l=0}^{\infty} f_{l0}^{c}(\kappa) Y_{l0}(\theta_{\boldsymbol{n}}, 0). \qquad (A14)$$

$f_{l0}^{c}(\kappa)$ can be determined by multiplying $Y_{l'0}^{*}(\theta_{\boldsymbol{n}}, 0)$ and integrating both sides, because of the standard orthogonality of the spherical harmonics.

$$f_{l0}^{c}(\kappa) = \int Y_{l0}^{*} f(\boldsymbol{n}|\hat{\boldsymbol{z}},\kappa) d\boldsymbol{n}$$

$$= \int \sqrt{\frac{2l+1}{4\pi}} P_l(cos\theta) \frac{1}{4\pi} \frac{e^{\kappa(\boldsymbol{\mu}\cdot\boldsymbol{n})}}{M\left(\frac{1}{2},\frac{3}{2},\kappa\right)} d\boldsymbol{n}$$

$$= \frac{1}{4\pi} \frac{1}{M\left(\frac{1}{2},\frac{3}{2},\kappa\right)} \int_0^{2\pi} sin\theta_{\boldsymbol{n}} d\phi_{\boldsymbol{n}} \int_0^{\pi} d\theta_{\boldsymbol{n}} \sqrt{\frac{2l+1}{4\pi}} P_l(cos\theta_{\boldsymbol{n}}) e^{\kappa cos^2\theta_{\boldsymbol{n}}}$$

$$= \frac{\sqrt{2l+1}}{4\sqrt{\pi} \cdot M\left(\frac{1}{2},\frac{3}{2},\kappa\right)} \int_{-1}^{1} dx\, P_l(x) e^{\kappa x^2} \qquad (A15)$$

Now, according to Arfken et al. (Arfken and Weber, 2005),

$$\int_{-1}^{1} P_l(\mu)\, e^{x\mu^2} = (x)^{l/2} \frac{\Gamma\left(\frac{l+1}{2}\right)}{\Gamma\left(\frac{2l+3}{2}\right)} M\left(\frac{l+1}{2}, \frac{2l+3}{2}, x\right). \qquad (A16)$$

Hence, $f_{l0}^{c}(\kappa)$ is expressed using Eq. (A15), (A16) as below:

$$f_{l0}^{c}(\kappa) = \frac{\sqrt{2l+1}}{4\sqrt{\pi}} \frac{\Gamma\left(\frac{l+1}{2}\right)}{\Gamma\left(\frac{2l+3}{2}\right)} \frac{M\left(\frac{l+1}{2}, \frac{2l+3}{2}, \kappa\right)}{M\left(\frac{1}{2},\frac{3}{2},\kappa\right)} (\kappa)^{l/2}. \qquad (A17)$$

In addition, it can be also applied for factors below, which $A_{ic}$ contains:

$$\int_{-1}^{1} dx\, P_l(x) e^{-bd_{\parallel}x^2} = (-bd_{\parallel})^{l/2} \frac{\Gamma\left(\frac{l+1}{2}\right)}{\Gamma\left(\frac{2l+3}{2}\right)} M\left(\frac{l+1}{2}, \frac{2l+3}{2}, -bd_{\parallel}\right). \qquad (A18)$$

In summary, $A_{ic}$ is expressed using Eq. (A13), (A17), (A18) as follows:

bioRxiv preprint doi: https://doi.org/10.1101/441659; this version posted October 13, 2018. The copyright holder for this preprint (which was not certified by peer review) is the author/funder, who has granted bioRxiv a license to display the preprint in perpetuity. It is made available under aCC-BY-NC-ND 4.0 International license.

$$A_{ic} = 2\pi \sum_{l=0}^{\infty} \frac{\sqrt{2l+1}}{4\sqrt{\pi}} \frac{\Gamma\left(\frac{l+1}{2}\right)}{\Gamma\left(\frac{2l+3}{2}\right)} \frac{M\left(\frac{l+1}{2}, \frac{2l+3}{2}, \kappa\right)}{M\left(\frac{1}{2}, \frac{3}{2}, \kappa\right)} (\kappa)^{l/2} \sqrt{\frac{2l+1}{4\pi}} P_l(cos\theta_q)(-bd_{\parallel})^{l/2} \frac{\Gamma\left(\frac{l+1}{2}\right)}{\Gamma\left(\frac{2l+3}{2}\right)} M\left(\frac{l+1}{2}, \frac{2l+3}{2}, -bd_{\parallel}\right)$$

$$= \frac{1}{4 \cdot M\left(\frac{1}{2}, \frac{3}{2}, \kappa\right)} \sum_{l=0}^{\infty} (2l+1) \left(\frac{\Gamma\left(\frac{l+1}{2}\right)}{\Gamma\left(\frac{2l+3}{2}\right)}\right)^2 P_l(cos\theta_q)(-bd_{\parallel}\kappa)^{l/2} M\left(\frac{l+1}{2}, \frac{2l+3}{2}, \kappa\right) M\left(\frac{l+1}{2}, \frac{2l+3}{2}, -bd_{\parallel}\right). \quad (A19)$$

Moreover, the sum of $l$ should be performed for only the even numbers, because the symmetry of θ direction of the Watson distribution.

## 4. The Watson distribution

According to the original NODDI model (Zhang et al., 2012), the Watson distribution is expressed as follows:

$$f(\boldsymbol{n}) = \frac{1}{M\left(\frac{1}{2}, \frac{3}{2}, \kappa\right)} e^{\kappa(\boldsymbol{\mu}\cdot\boldsymbol{n})^2}, \quad (A20)$$

where M is the first type confluent hypergeometric function (Arfken and Weber, 2005) and is also referred to as Kummer function. Here, $\boldsymbol{\mu}$, $\kappa$ and $\boldsymbol{n}$ are denoted as the mean orientation of the Watson distribution, concentration parameter, and the orientation of sticks in which water diffusion is restricted, respectively. Since the Watson distribution is also a function of $\boldsymbol{\mu}$ and $\kappa$, these variables are expressed as $f(\boldsymbol{n}) = f(\boldsymbol{n}|\boldsymbol{\mu}, \kappa)$.

Let $\boldsymbol{\mu} = \hat{\boldsymbol{z}}$ (unit vector in the z direction) and let $x = cos\theta$, $dx = -sin\theta \cdot d\theta$, we integrate over unit sphere $\mathbb{S}^2$.

$$\int_{\mathbb{S}^2} f(\boldsymbol{n}|\hat{\boldsymbol{z}}, \boldsymbol{\kappa}) d\boldsymbol{n} = \frac{1}{M\left(\frac{1}{2}, \frac{3}{2}, \kappa\right)} \int_{\mathbb{S}^2} e^{\kappa(\hat{\boldsymbol{z}}\cdot\boldsymbol{n})^2} d\boldsymbol{n}$$

$$= \frac{1}{M\left(\frac{1}{2}, \frac{3}{2}, \kappa\right)} \int_0^{2\pi} sin\theta d\phi \int_0^{\pi} d\theta \cdot e^{\kappa(cos\theta)^2}$$

$$= \frac{1}{M\left(\frac{1}{2}, \frac{3}{2}, \kappa\right)} \cdot 2\pi \cdot \int_{-1}^{1} e^{\kappa x^2} dx. \quad (A21)$$

According to Arfken and Wever (2005),

$$\int_{-1}^{1} P_l(\mu)\, e^{x\mu^2} = (x)^{l/2} \frac{\Gamma\left(\frac{l+1}{2}\right)}{\Gamma\left(\frac{2l+3}{2}\right)} M\left(\frac{l+1}{2}, \frac{2l+3}{2}, x\right), \quad (A22)$$

where $\Gamma(x)$ is Gamma function, $\Gamma(1/2) = \sqrt{\pi}$, $\Gamma(3/2) = \sqrt{\pi}/2$.

Hence, Eq. A21 is expressed using Eq. (A22) as follows:

bioRxiv preprint doi: https://doi.org/10.1101/441659; this version posted October 13, 2018. The copyright holder for this preprint (which was not certified by peer review) is the author/funder, who has granted bioRxiv a license to display the preprint in perpetuity. It is made available under aCC-BY-NC-ND 4.0 International license.

$$\int_{\mathbb{S}^2} f(\boldsymbol{n}|\hat{\boldsymbol{z}},\boldsymbol{\kappa})d\boldsymbol{n} = \frac{1}{M\left(\frac{1}{2},\frac{3}{2},\kappa\right)} \cdot 2\pi \cdot (\kappa)^{0/2} \frac{\Gamma\left(\frac{1}{2}\right)}{\Gamma\left(\frac{3}{2}\right)} M\left(\frac{1}{2},\frac{3}{2},\kappa\right)$$

$$= 4\pi. \qquad (A23)$$

Since we want to normalize the Watson distribution, we re-defined it as follows:

$$f(\boldsymbol{n}|\boldsymbol{\mu},\kappa) = \frac{1}{4\pi \cdot M\left(\frac{1}{2},\frac{3}{2},\kappa\right)} e^{\kappa(\boldsymbol{\mu}\cdot\boldsymbol{n})^2}. \qquad (A24)$$

## References

A Morrison, M., and A Parker, G. (1987). A Guide to Rotations in Quantum Mechanics. *Aust. J. Phys.* 40, 465. doi:10.1071/PH870465.

Adluru, G., Gur, Y., Anderson, J. S., Richards, L. G., Adluru, N., and DiBella, E. V. R. (2014). Assessment of white matter microstructure in stroke patients using NODDI. in (IEEE), 742–745. doi:10.1109/EMBC.2014.6943697.

Arfken, G. B., and Weber, H. J. eds. (2005). "Front Matter," in *Mathematical Methods for Physicists (6th Edition)* (Boston: Academic Press), 1200.

Assaf, Y. (2018). Imaging laminar structures in the gray matter with diffusion MRI. *NeuroImage*. doi:10.1016/j.neuroimage.2017.12.096.

Basser, P. J., Mattiello, J., and Lebihan, D. (1994a). Estimation of the Effective Self-Diffusion Tensor from the NMR Spin Echo. *J. Magn. Reson. B* 103, 247–254. doi:10.1006/jmrb.1994.1037.

Basser, P. J., Mattiello, J., and LeBihan, D. (1994b). MR diffusion tensor spectroscopy and imaging. *Biophys. J.* 66, 259–267. doi:10.1016/S0006-3495(94)80775-1.

Behrens, T. E. J., Woolrich, M. W., Jenkinson, M., Johansen-Berg, H., Nunes, R. G., Clare, S., et al. (2003). Characterization and propagation of uncertainty in diffusion-weighted MR imaging. *Magn. Reson. Med.* 50, 1077–1088. doi:10.1002/mrm.10609.

Billiet, T., Mädler, B., D'Arco, F., Peeters, R., Deprez, S., Plasschaert, E., et al. (2014). Characterizing the microstructural basis of "unidentified bright objects" in neurofibromatosis type 1: A combined in vivo multicomponent T2 relaxation and multi-shell diffusion MRI analysis. *NeuroImage Clin.* 4, 649–658. doi:10.1016/j.nicl.2014.04.005.

Billiet, T., Vandenbulcke, M., Mädler, B., Peeters, R., Dhollander, T., Zhang, H., et al. (2015). Age-related microstructural differences quantified using myelin water imaging and advanced diffusion MRI. *Neurobiol. Aging* 36, 2107–2121. doi:10.1016/j.neurobiolaging.2015.02.029.

Bland, J. M., and Altman, D. (1986). STATISTICAL METHODS FOR ASSESSING AGREEMENT BETWEEN TWO METHODS OF CLINICAL MEASUREMENT. *The Lancet* 327,

bioRxiv preprint doi: https://doi.org/10.1101/441659; this version posted October 13, 2018. The copyright holder for this preprint (which was not certified by peer review) is the author/funder, who has granted bioRxiv a license to display the preprint in perpetuity. It is made available under aCC-BY-NC-ND 4.0 International license.

307–310. doi:10.1016/S0140-6736(86)90837-8.

Bland, J. M., and Altman, D. G. (2003). Applying the right statistics: analyses of measurement studies. *Ultrasound Obstet. Gynecol.* 22, 85–93.

Burdette, J. H., Durden, D. D., Elster, A. D., and Yen, Y. F. (2001). High b-value diffusion-weighted MRI of normal brain. *J. Comput. Assist. Tomogr.* 25, 515–519.

Calabrese, M., Rinaldi, F., Seppi, D., Favaretto, A., Squarcina, L., Mattisi, I., et al. (2011). Cortical Diffusion-Tensor Imaging Abnormalities in Multiple Sclerosis: A 3-year Longitudinal Study. *Radiology* 261, 891–898. doi:10.1148/radiol.11110195.

Chang, Y. S., Owen, J. P., Pojman, N. J., Thieu, T., Bukshpun, P., Wakahiro, M. L. J., et al. (2015). White Matter Changes of Neurite Density and Fiber Orientation Dispersion during Human Brain Maturation. *PLOS ONE* 10, e0123656. doi:10.1371/journal.pone.0123656.

Chou, M.-C., Lin, Y.-R., Huang, T.-Y., Wang, C.-Y., Chung, H.-W., Juan, C.-J., et al. (2005). FLAIR Diffusion-Tensor MR Tractography: Comparison of Fiber Tracking with Conventional Imaging. *Am. J. Neuroradiol.* 26, 591–597.

Daducci, A., Canales-Rodríguez, E. J., Zhang, H., Dyrby, T. B., Alexander, D. C., and Thiran, J.-P. (2015). Accelerated Microstructure Imaging via Convex Optimization (AMICO) from diffusion MRI data. *NeuroImage* 105, 32–44. doi:10.1016/j.neuroimage.2014.10.026.

DeLano, M. C., Cooper, T. G., Siebert, J. E., Potchen, M. J., and Kuppusamy, K. (2000). High-b-value Diffusion-weighted MR Imaging of Adult Brain: Image Contrast and Apparent Diffusion Coefficient Map Features. *Am. J. Neuroradiol.* 21, 1830–1836.

Dowell, N. G., Bouyagoub, S., Tibble, J., Voon, V., Cercignani, M., and Harrison, N. A. (2017). Interferon-alpha-Induced Changes in NODDI Predispose to the Development of Fatigue. *Neuroscience*. doi:10.1016/j.neuroscience.2017.12.040.

Eaton-Rosen, Z., Melbourne, A., Orasanu, E., Cardoso, M. J., Modat, M., Bainbridge, A., et al. (2015). Longitudinal measurement of the developing grey matter in preterm subjects using multi-modal MRI. *NeuroImage* 111, 580–589. doi:10.1016/j.neuroimage.2015.02.010.

Edwards, L. J., Pine, K. J., Ellerbrock, I., Weiskopf, N., and Mohammadi, S. (2017). NODDI-DTI: Estimating Neurite Orientation and Dispersion Parameters from a Diffusion Tensor in Healthy White Matter. *Front. Neurosci.* 11. doi:10.3389/fnins.2017.00720.

Eustache, P., Nemmi, F., Saint-Aubert, L., Pariente, J., and Péran, P. (2016). Multimodal Magnetic Resonance Imaging in Alzheimer's Disease Patients at Prodromal Stage. *J. Alzheimers Dis.* 50, 1035–1050. doi:10.3233/JAD-150353.

Farrell, J. A. D., Landman, B. A., Jones, C. K., Smith, S. A., Prince, J. L., van Zijl, P. C. M., et al. (2007). Effects of signal-to-noise ratio on the accuracy and reproducibility of diffusion tensor

bioRxiv preprint doi: https://doi.org/10.1101/441659; this version posted October 13, 2018. The copyright holder for this preprint (which was not certified by peer review) is the author/funder, who has granted bioRxiv a license to display the preprint in perpetuity. It is made available under aCC-BY-NC-ND 4.0 International license.

imaging–derived fractional anisotropy, mean diffusivity, and principal eigenvector measurements at 1.5T. *J. Magn. Reson. Imaging* 26, 756–767. doi:10.1002/jmri.21053.

Fukutomi, H., Glasser, M. F., Zhang, H., Autio, J. A., Coalson, T. S., Okada, T., et al. (2018). Neurite imaging reveals microstructural variations in human cerebral cortical gray matter. *NeuroImage*. doi:10.1016/j.neuroimage.2018.02.017.

Genc, S., Malpas, C. B., Holland, S. K., Beare, R., and Silk, T. J. (2017). Neurite density index is sensitive to age related differences in the developing brain. *NeuroImage* 148, 373–380. doi:10.1016/j.neuroimage.2017.01.023.

Glasser, M. F., Coalson, T. S., Robinson, E. C., Hacker, C. D., Harwell, J., Yacoub, E., et al. (2016). A multi-modal parcellation of human cerebral cortex. *Nature* 536, 171–178. doi:10.1038/nature18933.

Glasser, M. F., Sotiropoulos, S. N., Wilson, J. A., Coalson, T. S., Fischl, B., Andersson, J. L., et al. (2013). The minimal preprocessing pipelines for the Human Connectome Project. *NeuroImage* 80, 105–124. doi:10.1016/j.neuroimage.2013.04.127.

Glasser, M. F., and Van Essen, D. C. (2011). Mapping human cortical areas in vivo based on myelin content as revealed by T1- and T2-weighted MRI. *J. Neurosci. Off. J. Soc. Neurosci.* 31, 11597–11616. doi:10.1523/JNEUROSCI.2180-11.2011.

Gonzalezballester, M. (2002). Estimation of the partial volume effect in MRI. *Med. Image Anal.* 6, 389–405. doi:10.1016/S1361-8415(02)00061-0.

Grussu, F., Schneider, T., Tur, C., Yates, R. L., Tachrount, M., Ianuş, A., et al. (2017). Neurite dispersion: a new marker of multiple sclerosis spinal cord pathology? *Ann. Clin. Transl. Neurol.* 4, 663–679. doi:10.1002/acn3.445.

Henf, J., Grothe, M. J., Brueggen, K., Teipel, S., and Dyrba, M. (2018). Mean diffusivity in cortical gray matter in Alzheimer's disease: The importance of partial volume correction. *NeuroImage Clin.* 17, 579–586. doi:10.1016/j.nicl.2017.10.005.

Hui, E. S., Cheung, M. M., Chan, K. C., and Wu, E. X. (2010). B-value dependence of DTI quantitation and sensitivity in detecting neural tissue changes. *NeuroImage* 49, 2366–2374. doi:10.1016/j.neuroimage.2009.10.022.

Jelescu, I. O., Veraart, J., Fieremans, E., and Novikov, D. S. (2016). Degeneracy in model parameter estimation for multi-compartmental diffusion in neuronal tissue: Degeneracy in Model Parameter Estimation of Diffusion in Neural Tissue. *NMR Biomed.* 29, 33–47. doi:10.1002/nbm.3450.

Johansen-Berg, H., and Behrens, T. (2013). Diffusion MRI: From Quantitative Measurement to In vivo Neuroanatomy: Second Edition. 1–614.

Jones, D. K. (2004). The effect of gradient sampling schemes on measures derived from diffusion

bioRxiv preprint doi: https://doi.org/10.1101/441659; this version posted October 13, 2018. The copyright holder for this preprint (which was not certified by peer review) is the author/funder, who has granted bioRxiv a license to display the preprint in perpetuity. It is made available under aCC-BY-NC-ND 4.0 International license.

tensor MRI: A Monte Carlo study. *Magn. Reson. Med.* 51, 807–815. doi:10.1002/mrm.20033.

Jones, D. K., and Basser, P. J. (2004). ?Squashing peanuts and smashing pumpkins?: How noise distorts diffusion-weighted MR data. *Magn. Reson. Med.* 52, 979–993. doi:10.1002/mrm.20283.

Jones, D. K., and Cercignani, M. (2010). Twenty-five pitfalls in the analysis of diffusion MRI data. *NMR Biomed.* 23, 803–820. doi:10.1002/nbm.1543.

Kaden, E., Kelm, N. D., Carson, R. P., Does, M. D., and Alexander, D. C. (2016). Multi-compartment microscopic diffusion imaging. *NeuroImage* 139, 346–359. doi:10.1016/j.neuroimage.2016.06.002.

Kodiweera, C., Alexander, A. L., Harezlak, J., McAllister, T. W., and Wu, Y.-C. (2016). Age effects and sex differences in human brain white matter of young to middle-aged adults: A DTI, NODDI, and q-space study. *NeuroImage* 128, 180–192. doi:10.1016/j.neuroimage.2015.12.033.

Kunz, N., Zhang, H., Vasung, L., O'Brien, K. R., Assaf, Y., Lazeyras, F., et al. (2014). Assessing white matter microstructure of the newborn with multi-shell diffusion MRI and biophysical compartment models. *NeuroImage* 96, 288–299. doi:10.1016/j.neuroimage.2014.03.057.

Kwong, K. K., McKinstry, R. C., Chien, D., Crawley, A. P., Pearlman, J. D., and Rosen, B. R. (1991). CSF-suppressed quantitative single-shot diffusion imaging. *Magn. Reson. Med.* 21, 157–163. doi:10.1002/mrm.1910210120.

Lampinen, B., Szczepankiewicz, F., Mårtensson, J., van Westen, D., Sundgren, P. C., and Nilsson, M. (2017). Neurite density imaging versus imaging of microscopic anisotropy in diffusion MRI: A model comparison using spherical tensor encoding. *NeuroImage* 147, 517–531. doi:10.1016/j.neuroimage.2016.11.053.

Marcus, D. S., Harms, M. P., Snyder, A. Z., Jenkinson, M., Wilson, J. A., Glasser, M. F., et al. (2013). Human Connectome Project informatics: Quality control, database services, and data visualization. *NeuroImage* 80, 202–219. doi:10.1016/j.neuroimage.2013.05.077.

Mardia, K. V., and Jupp, P. E. eds. (1990). *Directional Statistics. Wiley Series in Probability and Statistics*. John Wiley & Sons, Ltd.

Moseley, M. E., Cohen, Y., Kucharczyk, J., Mintorovitch, J., Asgari, H. S., Wendland, M. F., et al. (1990). Diffusion-weighted MR imaging of anisotropic water diffusion in cat central nervous system. *Radiology* 176, 439–445. doi:10.1148/radiology.176.2.2367658.

Nazeri, A., Chakravarty, M. M., Rotenberg, D. J., Rajji, T. K., Rathi, Y., Michailovich, O. V., et al. (2015). Functional Consequences of Neurite Orientation Dispersion and Density in Humans across the Adult Lifespan. *J. Neurosci.* 35, 1753–1762. doi:10.1523/JNEUROSCI.3979-14.2015.

Nazeri, A., Mulsant, B. H., Rajji, T. K., Levesque, M. L., Pipitone, J., Stefanik, L., et al. (2016). Gray Matter Neuritic Microstructure Deficits in Schizophrenia and Bipolar Disorder. *Biol.*

bioRxiv preprint doi: https://doi.org/10.1101/441659; this version posted October 13, 2018. The copyright holder for this preprint (which was not certified by peer review) is the author/funder, who has granted bioRxiv a license to display the preprint in perpetuity. It is made available under aCC-BY-NC-ND 4.0 International license.

*Psychiatry*. doi:10.1016/j.biopsych.2016.12.005.

Panagiotaki, E., Schneider, T., Siow, B., Hall, M. G., Lythgoe, M. F., and Alexander, D. C. (2012). Compartment models of the diffusion MR signal in brain white matter: A taxonomy and comparison. *NeuroImage* 59, 2241–2254. doi:10.1016/j.neuroimage.2011.09.081.

Papadakis, N. G., Xing, D., Houston, G. C., Smith, J. M., Smith, M. I., James, M. F., et al. (1999). A study of rotationally invariant and symmetric indices of diffusion anisotropy. *Magn. Reson. Imaging* 17, 881–892. doi:10.1016/S0730-725X(99)00029-6.

Pierpaoli, C., and Basser, P. J. (1996). Toward a quantitative assessment of diffusion anisotropy. *Magn. Reson. Med.* 36, 893–906. doi:10.1002/mrm.1910360612.

Pierpaoli, C., Jezzard, P., Basser, P. J., Barnett, A., and Di Chiro, G. (1996). Diffusion tensor MR imaging of the human brain. *Radiology* 201, 637–648. doi:10.1148/radiology.201.3.8939209.

Robinson, E. C., Garcia, K., Glasser, M. F., Chen, Z., Coalson, T. S., Makropoulos, A., et al. (2018). Multimodal surface matching with higher-order smoothness constraints. *NeuroImage* 167, 453–465. doi:10.1016/j.neuroimage.2017.10.037.

Robinson, E. C., Jbabdi, S., Glasser, M. F., Andersson, J., Burgess, G. C., Harms, M. P., et al. (2014). MSM: a new flexible framework for Multimodal Surface Matching☆. *NeuroImage* 100, 414. doi:10.1016/j.neuroimage.2014.05.069.

Rosenberg, G. A., Kyner, W. T., and Estrada, E. (1980). Bulk flow of brain interstitial fluid under normal and hyperosmolar conditions. *Am. J. Physiol.-Ren. Physiol.* 238, F42–F49. doi:10.1152/ajprenal.1980.238.1.F42.

Sato, K., Kerever, A., Kamagata, K., Tsuruta, K., Irie, R., Tagawa, K., et al. (2017). Understanding microstructure of the brain by comparison of neurite orientation dispersion and density imaging (NODDI) with transparent mouse brain. *Acta Radiol. Open* 6, 205846011770381. doi:10.1177/2058460117703816.

Schilling, K. G., Janve, V., Gao, Y., Stepniewska, I., Landman, B. A., and Anderson, A. W. (2018). Histological validation of diffusion MRI fiber orientation distributions and dispersion. *NeuroImage* 165, 200–221. doi:10.1016/j.neuroimage.2017.10.046.

Shrout, P. E., and Fleiss, J. L. (1979). Intraclass correlations: Uses in assessing rater reliability. *Psychol. Bull.* 86, 420–428. doi:10.1037/0033-2909.86.2.420.

Song, Y., Li, X., Huang, X., Zhao, J., Zhou, X., Wang, Y., et al. (2017). A study of neurite orientation dispersion and density imaging in wilson's disease: NODDI Application in Wilson's Disease. *J. Magn. Reson. Imaging*. doi:10.1002/jmri.25930.

Sotiropoulos, S. N., Behrens, T. E. J., and Jbabdi, S. (2012). Ball and rackets: Inferring fiber fanning from diffusion-weighted MRI. *NeuroImage* 60, 1412–1425. doi:10.1016/j.neuroimage.2012.01.056.

bioRxiv preprint doi: https://doi.org/10.1101/441659; this version posted October 13, 2018. The copyright holder for this preprint (which was not certified by peer review) is the author/funder, who has granted bioRxiv a license to display the preprint in perpetuity. It is made available under aCC-BY-NC-ND 4.0 International license.

Sotiropoulos, S. N., Jbabdi, S., Xu, J., Andersson, J. L., Moeller, S., Auerbach, E. J., et al. (2013). Advances in diffusion MRI acquisition and processing in the Human Connectome Project. *NeuroImage* 80, 125–143. doi:10.1016/j.neuroimage.2013.05.057.

Timmers, I., Zhang, H., Bastiani, M., Jansma, B. M., Roebroeck, A., and Rubio-Gozalbo, M. E. (2015). White matter microstructure pathology in classic galactosemia revealed by neurite orientation dispersion and density imaging. *J. Inherit. Metab. Dis.* 38, 295–304. doi:10.1007/s10545-014-9780-x.

Triarhou, L. C. ed. (2009). *Cellular Structure of the Human Cerebral Cortex: Translated and edited by L.C. Triarhou (Thessaloniki) Plus poster: "The 107 Cortical Cytoarchitectonic Areas of Constantin von Economo and Georg N. Koskinas in the Adult Human Brain."* S. Karger AG doi:10.1159/isbn.978-3-8055-9062-4.

Vaz, S., Falkmer, T., Passmore, A. E., Parsons, R., and Andreou, P. (2013). The Case for Using the Repeatability Coefficient When Calculating Test–Retest Reliability. *PLoS ONE* 8, e73990–7.

von Economo, C., and Koskinas (1925). *Die Cytoarchitektonik der Hirnrinde des erwachsenen Menschen. Textband. Verlag von Julius Springer, Berlin.*

Winston, G. P., Micallef, C., Symms, M. R., Alexander, D. C., Duncan, J. S., and Zhang, H. (2014). Advanced diffusion imaging sequences could aid assessing patients with focal cortical dysplasia and epilepsy. *Epilepsy Res.* 108, 336–339. doi:10.1016/j.eplepsyres.2013.11.004.

Zhang, H., Schneider, T., Wheeler-Kingshott, C. A., and Alexander, D. C. (2012). NODDI: Practical in vivo neurite orientation dispersion and density imaging of the human brain. *NeuroImage* 61, 1000–1016. doi:10.1016/j.neuroimage.2012.03.072.